表1　Wntシグナルに関する遺伝子改変マウスの表現型

| 遺伝子改変マウスの名称 | Wntシグナルの変化 | 膵臓・膵外分泌細胞・膵内分泌細胞の表現型 | 耐糖能異常の有無 | 文献番号 |
|---|---|---|---|---|
| Pdx1-Wnt1-Tg | 亢進 | 膵臓の無形成 | 記載なし | 10 |
| Pdx1-Wnt5a-Tg | 亢進 | 膵臓の低形成 | 記載なし | 10 |
| Pdx1-Frz8CRD-Tg | 低下 | 膵臓の低形成<br>内分泌細胞に大きな異常なし | 耐糖能異常なし | 12 |
| LRP5-/- | 低下 | 膵島の大きさに変化なし | 耐糖能異常あり | 13 |
| Pdx1-early-βcat-active | 亢進 | 膵臓の無形成 | 記載なし | 11 |
| Pdx1-late-βcat-active | 亢進 | 膵臓の大型化<br>外分泌細胞の増加 | 耐糖能異常なし | 11 |
| Pdx1-βcat-cKO | 低下 | *報告者により異なる<br>膵臓：変化なし～低形成<br>外分泌細胞：減少<br>内分泌細胞/膵β細胞：<br>変化なし～減少 | *報告者により異なる<br>耐糖能異常なし～あり | 14～17 |
| RIP-βcat-cKO | 低下 | 膵β細胞量の減少 | 耐糖能異常あり | 18 |
| Tcf7l2-/- | 低下 | 出生後間もなく死亡するが<br>膵β細胞量に変化なし | 肝臓での糖新生低下<br>により低血糖をきたす | 19, 20 |
| RIP-ERT2-Tcf7l2-cKO | 低下 | 成体で膵島の大きさに変化なし | 耐糖能異常なし | 20 |
| Pdx1-Tcf7l2-cKO | 低下 | 通常食では膵臓や膵島の<br>大きさに変化なし<br>高脂肪食負荷時では<br>膵β細胞量の増加が不十分 | 耐糖能異常あり | 21 |
| RIP-DNTcf7l2-Tg | 低下 | 出生直後・成体で<br>膵β細胞量の減少 | 耐糖能異常あり | 22 |

り，出生直後に死亡すると報告されている[19]．つい最近，本マウスでは，出生直後の膵β細胞量は野生型マウスと比較して変化がなく，膵β細胞の発生・分化・増殖にTcf7l2は必須ではないと報告されている[20]．また，HMG boxをコードするエクソンを欠損することが可能なfloxマウスとRIP-Cre-ERT2マウスを交配し，離乳後にタモキシフェンを投与することで，成体で膵β細胞特異的にTcf7l2を欠損させたマウス（RIP-ERT2-Tcf7l2-cKO）でも，膵島の大きさに変化はなく，耐糖能に異常はないと報告されている[20]．

一方で，βカテニン結合部位をコードするエクソンを欠損することが可能なfloxマウスとPdx-1Creマウスを交配して，胎生期から膵臓特異的にTcf7l2を欠損させたマウス（Pdx1-Tcf7l2-cKO）は，成体において膵臓や膵島の大きさに変化はないものの，インスリン分泌低下を伴う耐糖能異常を示し，高脂肪食負荷時の膵β細胞量の増加が不十分であったと報告されている[21]．両者の表現型が一致しない原因としては，ターゲットとするエクソンや使用するCreマウスの違いや，他のTcfファミリー蛋白質による代償機構の存在が考えられる．

また，最近われわれはインスリンプロモーターを用いて，N末端のβカテニン結合ドメインを欠失したdominant negative formのTcf7l2を膵β細胞で過剰発現させたマウス（RIP-DNTcf7l2-Tg）を作製し，表現型を解析している[22]．RIP-DNTcf7l2-Tgマウスは，糖負荷試験でインスリン分泌低下を伴う耐糖能異常を呈し，膵組織像での膵β細胞面積の減少と膵臓インスリン含量の減少を認め，出生直後時点でも，成体と同様に膵組織像での膵β細胞面積の減少と膵臓インスリン含量の減少を認めている．本マウスでは，胎生期よりdominant negative formのTcf7l2が過剰に発現することから，他のTcfファミリー蛋白質による代償機構が働かず，Tcf7l2を単独で欠損させた場合とは異なる表現型が観察される可能性があるものと考えられる．

ヒト膵島では多様なTcf7l2のスプライシングバリアントが発現しており，スプライシングバリアントによっては膵β細胞の増殖や機能に正反

対の作用を有することが報告されている[23]．したがって，Tcf7l2のSNPや病態によってスプライスバリアントの発現のパターンが変わる可能性が考えられ，リスクアリルのSNPの保有者や2型糖尿病では，膵β細胞の分化・増殖や機能を負に制御する作用を有するTcf7l2のスプライシングバリアントが膵島で増加しているのかもしれない．

## おわりに

Wntシグナルは，発生・分化に対して，そのタイミングにより「正」と「負」の相反する作用をもたらすものと考えられる．これまでに作製された遺伝子改変マウスで観察された表現型から，Wntシグナルと膵内分泌細胞の分化に関して，単純な結論を導くことは難しい(表1)．しかしながら，発生初期からの過剰なWntシグナルは膵臓の発生そのものを抑制することと，胎生期におけるWntシグナルの低下は膵外分泌細胞の分化・増殖を抑制することは，おおむね一致している点であると考えられる．

また，Wntシグナルは，βカテニンとTcfファミリー蛋白質を介して，膵内分泌細胞の分化・増殖に対して促進的に作用する可能性が示唆されるが，いまだ議論の余地がある．遺伝子改変マウスを用いた検討に加えて，実際にヒトの膵島や胎生期の膵臓で，βカテニンやTcfファミリー蛋白質がどのような挙動を示すのかを明らかにすることが，今後の重要な検討課題になると思われる．

## 文　献


1) Murtaugh LC. The what, where, when and how of Wnt/ β-catenin signaling in pancreas development. Organogenesis 2008 ; 4 : 81.
2) Liu Z, Habener JF. Wnt signaling in pancreatic islets. Adv Exp Med Biol 2010 ; 654 : 391.
3) 菊池　章．Wntシグナルネットワークとその異常による病態．生化学 2009；81：780.
4) Grant SF, Thorleifsson G, Reynisdottir I, et al. Variant of transcription factor 7-like 2 (TCF7L2) gene confers risk of type 2 diabetes. Nat Genet 2006 ; 38 : 320.
5) Horikoshi M, Hara K, Ito C, et al. A genetic variation of the transcription factor 7-like 2 gene is associated with risk of type 2 diabetes in the Japanese population. Diabetologia 2007 ; 50 : 747.
6) Hoppler S, Kavanagh CL. Wnt signalling : variety at the core. J Cell Sci 2007 ; 120 : 385.
7) Arce L, Yokoyama NN, Waterman ML. Diversity of LEF/TCF action in development and disease. Oncogene 2006 ; 25 : 7492.
8) Vacik T, Lemke G. Dominant-negative isoforms of Tcf/Lef proteins in development and disease. Cell Cycle 2011 ; 10 : 4199.
9) Vacik T, Stubbs JL, Lemke G. A novel mechanism for the transcriptional regulation of Wnt signaling in development. Genes Dev 2011 ; 25 : 1783.
10) Heller RS, Dichmann DS, Jensen J, et al. Expression patterns of Wnts, Frizzleds, sFRPs, and misexpression in transgenic mice suggesting a role for Wnts in pancreas and foregut pattern formation. Dev Dyn 2002 ; 225 : 260.
11) Heiser PW, Lau J, Taketo MM, et al. Stabilization of beta-catenin impacts pancreas growth. Development 2006 ; 133 : 2023.
12) Papadopoulou S, Edlund H. Attenuated Wnt signaling perturbs pancreatic growth but not pancreatic function. Diabetes 2005 ; 54 : 2844.
13) Fujino T, Asaba H, Kang MJ, et al. Low-density lipoprotein receptor-related protein 5 (LRP5) is essential for normal cholesterol metabolism and glucose-induced insulin secretion. Proc Natl Acad Sci USA 2003 ; 100 : 229.
14) Dessimoz J, Bonnard C, Huelsken J, Grapin-Botton A. Pancreas-specific deletion of beta catenin reveals Wnt-dependent and Wnt-independent functions during development. Curr Biol 2005 ; 15 : 1677.
15) Murtaugh LC, Law AC, Dor Y, Melton DA. Beta-Catenin is essential for pancreatic acinar but not islet development. Development 2005 ; 132 : 4663.
16) Wells JM, Esni F, Boivin GP J, et al. Wnt/beta-catenin signaling is required for development of the exocrine pancreas. BMC Dev Biol 2007 ; 7 : 4.
17) Elghazi L, Gould AP, Weiss AJ, et al. Importance of β-Catenin in glucose and energy homeostasis. Sci

Rep 2012 ; 2 : 693.
18) Dabernat S, Secrest P, Peuchant E, et al. Lack of beta-catenin in early life induces abnormal glucose homeostasis in mice. Diabetologia 2009 ; 52 : 1608.
19) Korinek V, Barker N, Moerer P, et al. Depletion of epithelial stem-cell compartments in the small intestine of mice lacking Tcf-4. Nat Genet 1998 ; 19 : 379.
20) Boj SF, van Es JH, Huch M, et al. Diabetes risk gene and Wnt effector Tcf7l2/TCF4 controls hepatic response to perinatal and adult metabolic demand. Cell 2012 ; 151 : 1595.
21) da Silva Xavier G, Mondragon A, Sun G, et al. Abnormal glucose tolerance and insulin secretion in pancreas-specific Tcf7l2-null mice. Diabetologia 2012 ; 55 : 2667.
22) Takamoto I, Kubota N, Kumagai K, et al. Role of Tcf7l2-mediated pathway in pancreatic beta cell in vivo. Diabetes 2012 ; 61 S1 : A30.
23) Le Bacquer O, Shu L, Marchand M, et al. TCF7L2 splice variants have distinct effects on beta-cell turnover and function. Hum Mol Genet 2011 ; 20 : 1906.

* * *

Structure
Article

# Tetrameric Interaction of the Ectoenzyme CD38 on the Cell Surface Enables Its Catalytic and Raft-Association Activities

Miki Hara-Yokoyama,[1,3,*] Mutsuko Kukimoto-Niino,[5] Kazue Terasawa,[1] Satoru Harumiya,[2] Katarzyna A. Podyma-Inoue,[1] Nobumasa Hino,[5] Kensaku Sakamoto,[5] Satsuki Itoh,[6] Noritaka Hashii,[6] Yoko Hiruta,[6] Nana Kawasaki,[6] Chiemi Mishima-Tsumagari,[5] Yoko Kaitsu,[5] Tomoko Matsumoto,[5] Motoaki Wakiyama,[5] Mikako Shirouzu,[5] Takeshi Kasama,[4] Hiroshi Takayanagi,[2,3,7] Naoko Utsunomiya-Tate,[10] Kiyoshi Takatsu,[11,12] Toshiaki Katada,[8] Yoshio Hirabayashi,[13] Shigeyuki Yokoyama,[5,9] and Masaki Yanagishita[1,3]

[1]Section of Biochemistry
[2]Section of Cell Signaling, Department of Hard Tissue Engineering, Graduate School of Medical and Dental Sciences
[3]The Global Center of Excellence (GCOE) Program, International Research Center for Molecular Sciences in Tooth and Bone Diseases
[4]Instrumental Analysis Research Division, Research Center for Medical and Dental Sciences
Tokyo Medical and Dental University, Tokyo 113-8549, Japan
[5]RIKEN Systems and Structural Biology Center, Yokohama, Kanagawa 230-0045, Japan
[6]Division of Biological Chemistry and Biologicals, National Institute of Health Science, Tokyo 158-8501, Japan
[7]Department of Immunology, Graduate School of Medicine and Faculty of Medicine
[8]Department of Physiological Chemistry, Graduate School of Pharmaceutical Sciences
[9]Department of Biophysics and Biochemistry, Graduate School of Science
University of Tokyo, Tokyo 113-0033, Japan
[10]Research Institute of Pharmaceutical Sciences, Musashino University, Tokyo 202-8585, Japan
[11]Toyama Prefectural Institute for Pharmaceutical Research, 17-1 Naka-Taikoyama, Imizu, Toyama 939-0363, Japan
[12]Department of Immunobiology and Pharmaceutical Genetics, Graduate School of Medicine and Pharmaceutical Science, University of Toyama, 2630 Sugitani, Toyama, Toyama 930-0194, Japan
[13]Brain Science Institute, The Institute of Physical and Chemical Research (RIKEN), Wako, Saitama 351-0198, Japan
*Correspondence: m.yokoyama.bch@tmd.ac.jp
http://dx.doi.org/10.1016/j.str.2012.06.017

## SUMMARY

**The leukocyte cell-surface antigen CD38 is the major nicotinamide adenide dinucleotide glycohydrolase in mammals, and its ectoenzyme activity is involved in calcium mobilization. CD38 is also a raft-dependent signaling molecule. CD38 forms a tetramer on the cell surface, but the structural basis and the functional significance of tetramerization have remained unexplored. We identified the interfaces contributing to the homophilic interaction of mouse CD38 by site-specific crosslinking on the cell surface with an expanded genetic code, based on a crystallographic analysis. A combination of the three interfaces enables CD38 to tetramerize: one interface involving the juxtamembrane α-helix is responsible for the formation of the core dimer, which is further dimerized via the other two interfaces. This dimerization of dimers is required for the catalytic activity and the localization of CD38 in membrane rafts. The glycosylation prevents further self-association of the tetramer. Accordingly, the tetrameric interaction underlies the multifaceted actions of CD38.**

## INTRODUCTION

The leukocyte cell-surface antigen CD38 is a glycoprotein, composed of a large extracellular domain, a transmembrane domain, and a short cytoplasmic domain (Jackson and Bell, 1990). The extracellular domain of CD38 contains the catalytic *nicotinamide adenide dinucleotide* ($NAD^+$) *glycohydrolase* (Gelman et al., 1993; Kontani et al., 1993), which is the main $NAD^+$ glycohydrolase in mammalian cells (Cockayne et al., 1998). The cleavage of the *N*-glycoside linkage of $NAD^+$ or nicotinamide adenine dinucleotide phosphate ($NADP^+$) generates ADP-ribose/cyclic ADP-ribose from $NAD^+$ and nicotinic acid adenine dinucleotide phosphate from $NADP^+$ (Malavasi et al., 2008). All of these products are able to trigger intracellular calcium mobilization in an inositol trisphosphate-independent manner, and CD38 thereby plays a role in calcium-mediated signaling (Lee, 1994, 2005). The catalytic activity of CD38 is required in various processes, such as insulin secretion (Kato et al., 1999; Takasawa et al., 1993), intracellular calcium oscillation (Fukushi et al., 2001), neutrophil chemotaxis (Partida-Sánchez et al., 2001), dendritic cell trafficking (Partida-Sánchez et al., 2004), and oxytocin secretion (Jin et al., 2007). CD38 is also involved in the development of diet-induced obesity via the activation of sirtuins, which are $NAD^+$-dependent deacetylases (Aksoy et al., 2006).

On the other hand, CD38 is concentrated in specialized membrane regions, such as the immunologic synapse (Muñoz et al., 2008) and membrane rafts (Malavasi et al., 2008). CD38 reportedly associates with various supramolecular complexes within membrane rafts in T cells (CD38/CD3/Lck/LAT) (Zubiaur et al., 1997), B cells (CD38/BCR/CD19/CD81) (Deaglio et al., 2003, 2007), natural killer cells (CD38/CD16) (Deaglio et al., 2002), monocytes (CD38/major histocompatibility complex [MHC] Class II/CD9) (Zilber et al., 2005), and mature dendritic

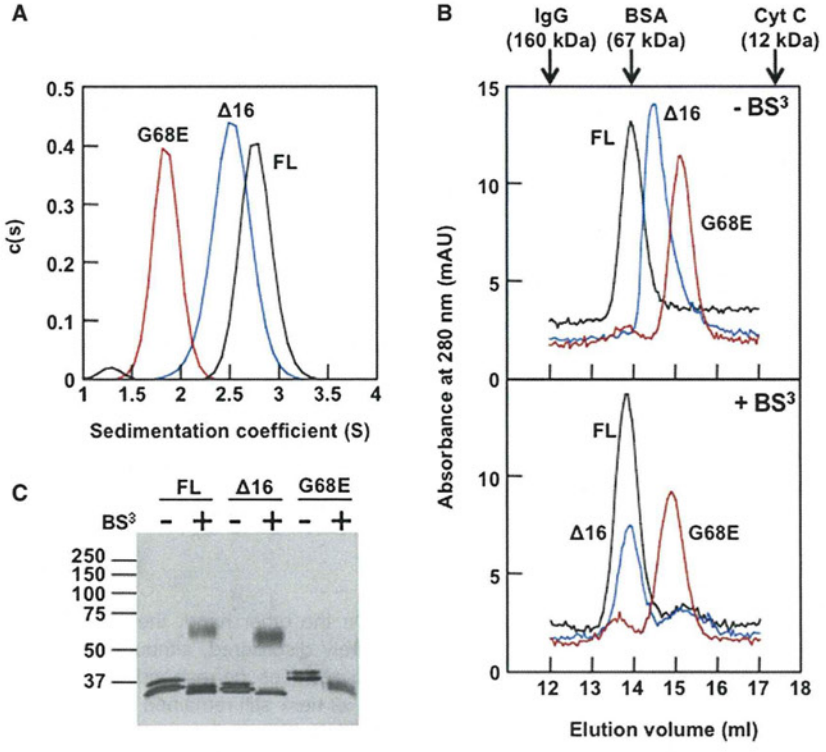


**Figure 1. Dimer Structure of the Isolated Extracellular Domain of CD38 in Solution**

(A and B) Sedimentation velocity experiments (A) and size-exclusion chromatography (B) were performed with the extracellular domain of CD38, without (full length [FL], black line, FLAG-tag at the N-terminal) or with the C-terminal truncation (Δ16, blue line, FLAG-tag at the N-terminal) or the G68E mutation (red line, FLAGx3-tag at the N-terminal), as described in the Supplemental Experimental Procedures.

(B and C) The extracellular domain of CD38 (0.1 mg/ml) was incubated in the absence and the presence of 200 μM $BS^3$ at room temperature for 2 hr. The proteins (2 μg each) were then subjected to 9% SDS-PAGE under reducing conditions and silver-stained (C). The presence of two bands without $BS^3$ is due to high-mannose moieties. See also Figure S1.

cells (CD38/CD83/CD11b/CD81) (Frasca et al., 2006). The association of CD38 with membrane rafts is independent of the catalytic activity of CD38 (Lund et al., 2006, 1999; Manjarrez-Orduño et al., 2007) and may be involved in the initiation of CD38-mediated signaling to trigger cell activation and proliferation.

The overall topology of the extracellular domain of human CD38 (Liu et al., 2005) is similar to those of the other members of the ADP-ribosyl cyclase family, i.e., *Aplysia* ADP-ribosyl cyclase (Prasad et al., 1996) and human bone marrow stromal cell antigen 1 (BST-1/CD157) (Yamamoto-Katayama et al., 2002). However, the three proteins differ from each other in terms of their membrane association. *Aplysia* ADP-ribosyl cyclase is cytosolic, while BST-1 and CD38 are membrane-bound via a glycosylphosphatidylinositol anchor and a transmembrane domain, respectively.

Biochemical and crystallographic analyses revealed that *Aplysia* ADP-ribosyl cyclase and a soluble form of BST-1 exist as dimers (Munshi et al., 1998; Sato et al., 1999). Interestingly, however, the existence of a tetrameric form of human CD38 has been demonstrated (Bruzzone et al., 1998; Franco et al., 1998; Mallone et al., 1998). Consistent with these reports, a high molecular weight form of CD38, corresponding to a tetramer, is induced by retinoic acid in human myeloid (HL-60) leukemia cells (Umar et al., 1996). It was suggested that the oligomerization is relevant to the catalytic activity of CD38 from porcine heart microsomes (Chidambaram et al., 1998). The orientation of the C-terminal α helix (α9) of human CD38 in the crystal is distinct from those of the other two members (Liu et al., 2005), so that the α9 helices would clash if two CD38 molecules formed a dimer in the same manner as the other two members (Figure S3B available online). Thus, CD38 may have a distinct homophilic interaction mode that enables tetramer formation on the cell surface. However, the structural aspects of CD38 assembly and their functional importance have not been elucidated thus far.

In the present study, we investigated the mechanism and the role of CD38 assembly. First, a crystallographic analysis of the extracellular domain of mouse CD38 revealed two interaction modes, whose combination allows the tetramerization of CD38 via a dimer-of-dimers assembly. Second, both interaction modes were actually found for cell-surface CD38 by a site-specific crosslinking experiment using an expanded genetic code. Third, the two interaction modes are both required for the catalytic activity and the targeting of mouse CD38 into membrane rafts. Accordingly, the present study provides the structural basis for the tetramerization of CD38 on the cell surface and demonstrates that the tetramerization of mouse CD38 is crucial for its multifaceted actions.

## RESULTS

### Novel Homophilic Interaction Modes of Mouse CD38 Deduced from the Crystal Packing of the Extracellular Domain

The full-length extracellular domain of mouse CD38 exists as a homodimer in solution, as revealed by analytical ultracentrifugation and size exclusion chromatography (Figure 1 and Figure S1). However, the homophilic interaction modes of CD38 were not suggested by the previous structural analysis of the full-length extracellular domain of human CD38, since the two molecules in the crystallographic unit lacked an apparent homodimer interface (Liu et al., 2005). In the present study, during the preparation of the extracellular domain of mouse CD38, we noticed that the protein was partially cleaved at F288, causing the truncation of 16 amino acid residues from the C terminus, representing half of the C-terminal α helix (Figure 2A). Thus, the crystal structure of the C-terminal-truncated extracellular domain was solved

 

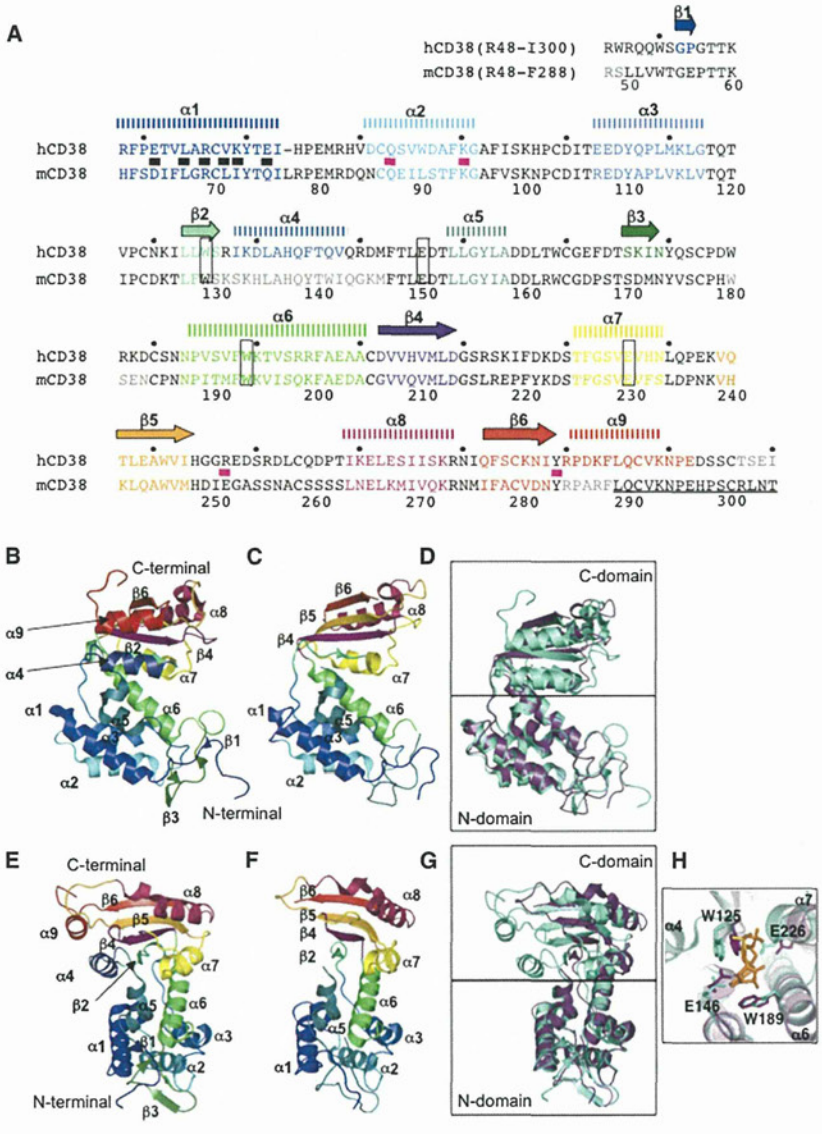


**Figure 2. The Crystal Structure of the C-Terminal Truncated Extracellular Domain of Mouse CD38**

(A) Sequence alignment between the extracellular domains of the human and mouse CD38 proteins. The truncation in mouse CD38 is underlined. The glycosylation sites were mutated. Catalytically important amino acid residues are boxed. The amino acid residues involving the type I and type II interfaces are indicated by black and pink bars, respectively.

(B, C, E, and F) Structures of the extracellular domain of the full-length human CD38, hCD38 (R48-I300) (B and E) and of the C-terminal truncated mouse CD38, mCD38mut(R48-F288) (C and F).

(D and G) Superimposition of the structures of hCD38(R48-I300) (green) and mCD38mut(R48-F288) (purple).

(H) An expanded view of the active sites. Cyclic inosine diphosphate-ribose is colored orange (2PGJ). See also Figure S2.

(accession code 2EG9; Table 1 and Figure 2) and four types of interfaces (I-IV) were found in the crystal packing (Figure 3).

The extracellular domain of CD38 with the C-terminal truncation also existed as a dimer in solution (Figure 1). The overall structure was not significantly altered by the truncation, based on the circular dichroism spectra (Figure S2). The crystal structure of the full-length extracellular domain of human CD38 (Liu et al., 2005) is divided into the N-domain (β1, α1, α2, α3, α5, β3, and α6) and the C-domain (β2, α4, β4, α7, β5, α8, β6, and α9). As shown in Figure 2, the crystal structure of the C-terminal-truncated extracellular domain of mouse CD38 revealed that the α helices (α1, α2, α3, α5, and α6) of the N-domain all superimposed well on those in the full-length extracellular domain. The two α helices (α7 and α8) and the three-stranded parallel β sheet (β4, β5, and β6) remain intact in the C-domain, and they are only slightly tilted, as compared with those in the full-length extracellular domain.

On the other hand, the α9 helix was entirely disordered, although the amino acid residues corresponding to half of the α9 helix still remained (Figure 2A). In addition, the region corresponding to the α4 helix of the full-length extracellular domain was also disordered (S130–M146) in the C-terminal-truncated form. Thus, the most notable consequence of the C-terminal truncation is the loss of the α9 helix and the fluctuation of the α4 helix.

The α1 helix exists at the type I interface. The α4 helix, which was not fully chain-traced, is actually located at the type III interface (Figure 3H). The edge of the α1 helix is in contact with the loop region between the β5 strand and the α8 helix at the type III interface. Although the type II interface between the α2 helix and the loop region between the β5 strand and the α8 helix by itself is too small to connect two CD38 molecules (Figure 3E), it may contribute to the oligomerization.

Based on the superimposition of the full-length extracellular domain of human CD38, the α4 and α9 helices are both located at the type III interface (Figure 3H). In this situation, the area of the type III interface is calculated to be 1473 Å$^2$. It is unlikely that the type IV interface exists in the cell-surface CD38, since the glycosylation precludes this interaction, as described below (Figure 6C). The combination of the type I and type II/III interfaces appears to cooperatively function in tetramer formation and is compatible with membrane association (Figure 6).

At the type I interface, hydrophilic interactions (D64•R69/R69•D64 and Q75•Q75) and hydrophobic interaction (D67•I72/I72•D67 and L71•L71) are formed between the α1 helices (Figure 3D). Hydrophilic interactions between Q87 and Y283 and between K94 and E251 are present at the type II interface

**Table 1. X-Ray Data Collection and Refinement Statistics**

| | |
|---|---|
| Data Collection | |
| Wavelength (Å) | 1.0 |
| Resolution (Å) | 50-2.8 (2.90-2.80) |
| Unique reflections | 11912 |
| Redundancy | 4.9 |
| Completeness (%) | 97.9 (95.5) |
| I / σ(I) | 11.6 (5.2) |
| $R_{sym}$[a] (%) | 9.8 (22.6) |
| Refinement | |
| Resolution (Å) | 49.12-2.80 |
| No. of reflections | 11873 |
| No. of protein atoms | 3390 |
| No. of water molecules | 23 |
| $R_{work}$ (%) | 26.3 |
| $R_{free}$ (%)[b] | 34.0 |
| rmsd bond length (Å) | 0.006 |
| rmsd bond angles (°) | 1.1 |

All numbers in parentheses represent last outer shell statistics.
[a] $R_{sym} = \Sigma\ |I_{avg}-Ii|\ /\ \Sigma Ii$, where $Ii$ is the observed intensity and $I_{avg}$ is the average intensity.
[b] $R_{free}$ is calculated for 10% of randomly selected reflections excluded from refinement.

(Figure 3G). These amino acid residues are either conserved or semi-conserved between mouse and human CD38 (Figure 2A). Thus, it is conceivable that the type I and type II interfaces are also possible for human CD38. Actually, an interface similar to type I was previously reported by Shi et al., in the crystal structure of the full-length extracellular domain of human CD38 (1ZVM), as shown in Figure S3C.

In the present study, the full-length extracellular domain of mouse CD38 was not successfully crystallized. For the crystallographic analyses, the glycosylation sites within the proteins were mutated as usual to avoid chemical heterogeneity. The nonglycosylated, full-length mouse CD38 forms a large, amorphous aggregate, probably due to the artificial interface IV, in addition to the three interfaces (types I-III). In contrast, the C-terminal truncation may have facilitated efficient crystal growth by avoiding amorphous aggregation through the weakening of the type III interface.

## The Type I Interaction Mode of the Extracellular Domain of CD38 Is Involved in Dimer Formation

The G68E mutation in the α1 helix reduces the stability of the homophilic interaction of mouse CD38, expressed in a murine pro B cell-derived cell line (Ba/F3 cells), after solubilization (Moreno-García et al., 2004). Here, the isolated extracellular domain with the G68E mutation was shown to be present as a monomer in solution by analytical ultracentrifugation and size exclusion chromatography (Figure 1 and Figure S1). According to the crystal structure, the G68E mutation should disrupt the type I interface (Figure 3D). Thus, the results support the interaction between the α1 helices of the extracellular domain of CD38 in solution (the type I interaction mode).

The full-length mouse CD38 on the cell surface was crosslinked by a membrane-impermeable, Lys-reactive chemical crosslinker, $BS^3$ (Moreno García et al., 2004). Actually, $BS^3$ treatment of the isolated extracellular domain of CD38 also converted it to a crosslinked dimer, which was abolished by the G68E mutation (Figure 1C). If the $BS^3$-crosslinking occurs via the type I interaction mode, then the candidate for the crosslinked site is Lys60-Lys60 (Figure S1). However, although trypsin does not cleave CD38 at the Lys residue that reacted with $BS^3$, efficient cleavage at Lys60 was detected when the tryptic fragments of the crosslinked dimer were analyzed by mass spectroscopy (Figure S1). Thus, it is unlikely that the $BS^3$-dependent crosslinking occurs via the type I interaction mode.

In the absence of the $BS^3$-treatment, the extracellular domain of CD38 with the C-terminal truncation eluted after the full-length extracellular domain during size exclusion chromatography, probably due to its smaller size (Figure 1B). However, the extracellular domains with and without the truncation eluted at the same position after the $BS^3$-dependent crosslinking, suggesting that the exposure of the C-terminal region to the solvent is avoided and the difference in the hydrodynamic property is counteracted by the crosslinking. In addition, the cleavage at Lys145 in the α4 helix was decreased when the crosslinked dimer was analyzed (Figure S1), implying that the $BS^3$-dependent intermolecular crosslinked via the type III interaction mode. Therefore, the dimer of the extracellular domains of CD38, formed via the type I interaction mode, is further considered to exist in equilibrium to form a tetramer via the type II/III interaction mode, within which the intermolecular $BS^3$-crosslinking occurs (Figure 3L).

## The Homophilic Interaction of CD38 on the Cell Surface

The $BS^3$-dependent intermolecular crosslinking of cell-surface CD38 was impaired by the G68E mutation and by the C-terminal truncation in A20 cells (Figures 4A and 4B). In addition, the loss of the conserved disulfide bridge, which stabilizes the C-terminal helix (C291A/C300A) (Figure 4C), reduced the intermolecular crosslinking (Figures 4D and 4E). It should be noted that covalently linked CD38 dimers were observed, even in the absence of $BS^3$, in the cases of the C291A and C300A mutations. Conceivably, the C-terminal helices can contact each other to permit the formation of artificial intermolecular disulfide bridges between Cys300-Cys300 and Cys291-Cys291 when the original disulfide bridge is disrupted and these residues lose their intramolecular partners. These results suggested that the C-terminal helix and the α1 helix are involved in the homophilic interaction of CD38 on the membrane, which supports the type I and type III interaction modes.

To confirm that the type I and type III interaction modes are actually involved in the CD38 assembly on the cell surface, a photo-reactive crosslinker, *p*-benzoyl-L-phenylalanine (*p*Bpa), was separately introduced into CD38 at a defined position, according to the method of Hino et al. (Hino et al., 2005, 2006). Among the 14 variants designed to evaluate the interfaces, three variants, with *p*Bpa in place of V292 in the α9 helix and D64 or I65 in the α1 helix, were sufficiently expressed in Chinese hamster ovary (CHO) cells and subjected to photo-crosslinking (Figure 5A). Crosslinked products with a molecular weight twice as large as that of one CD38 molecule were formed for the CD38 variants with *p*Bpa in place of V292, D64, and I65 (Figure 5B).

 

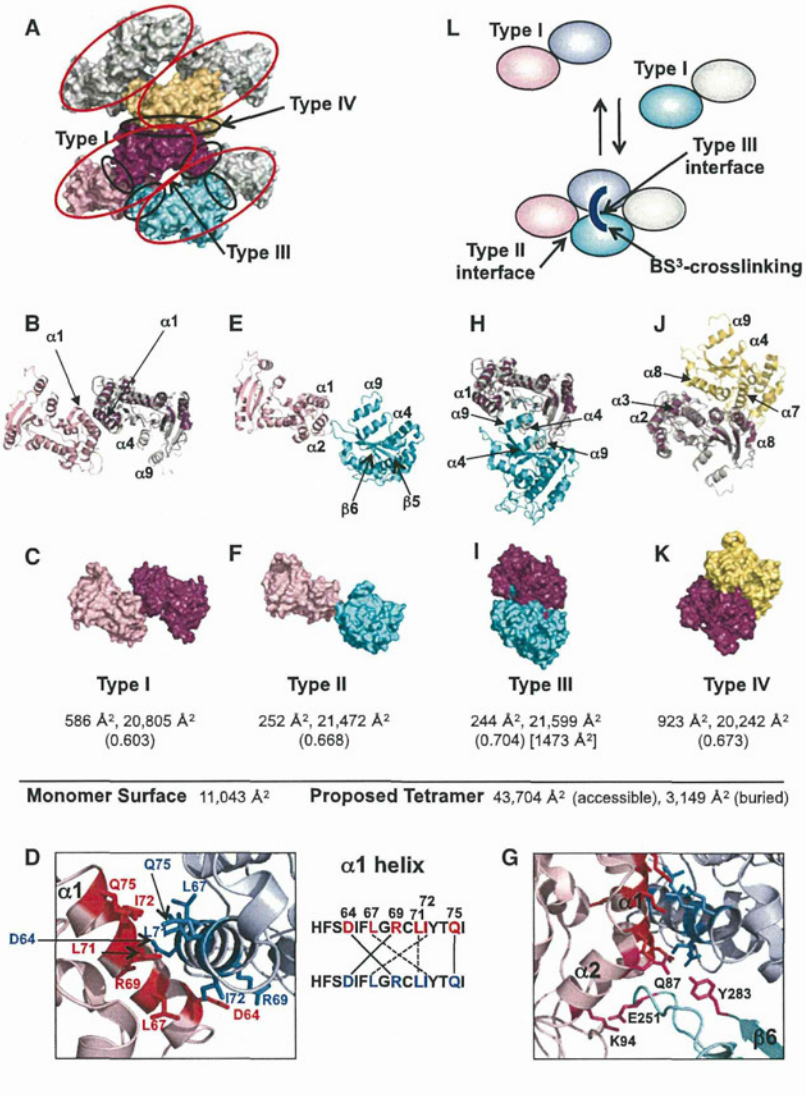


**Figure 3. The Interfaces Involved in the Homophilic Interaction of CD38**

(A) The crystal packing of mCD38mut(R48-F288) with asymmetric units (red) (2EG9).

(B, E, H, and J) Two molecules of the full-length extracellular domain, hCD38(R48-I300), oriented according to those in mCD38mut(R48-F288) (2EG9), are shown. The monomer structure of mCD38mut(R48-F288) (2EG9) was superimposed (purple).

(C, F, I, and K) The four types of interfaces (I-IV) are depicted with the accessible area and the shape complementarities (in parentheses).

(D and G) Expanded views of the type I and type II interfaces, respectively. Possible electrostatic (solid lines) and hydrophobic (dashed lines) interactions between the two α1 helices are shown in (D).

(L) The proposed dynamic equilibrium of the extracellular domain of CD38 in solution. See also Figure S3.

In order to confirm that the crosslinked products represent homophilic CD38 multimers, FLAG-tagged CD38 and Myc-tagged CD38 were coexpressed in CHO cells. The crosslinked products that were immunoprecipitated with the anti-FLAG antibody reacted with both the anti-FLAG and anti-Myc antibodies (Figures 5C and 5D, respectively). Thus, the results indicated that the crosslinking occurs between CD38 molecules and at least the α9 and α1 helices are near the interface. The detection of the products corresponding to the tetramer (Figures 5C and 5D) suggested that tetramerization of CD38 occurs on the cell surface and that the tetramer appears to be more stable than the isolated extracellular domain in solution.

## The Processing of the N-Glycan of CD38 Is Compatible with Tetramerization

During protein synthesis, oligomannose glycans are first processed by α-glucosidases and mannosidases in the endoplasmic reticulum and then are further processed to complex- or hybrid-type oligosaccharides by *N*-acetylglucosaminyltransferase I in the *medial*-Golgi (Figure S5A) (Kato and Kamiya, 2007). An analysis of the site-specific glycan of CD38 unexpectedly revealed that only the oligosaccharides attached to the N213 residue remained as the high-mannose-type (Figure S5B). Within the CD38 tetramer, the N213 residue faces the space between the extracellular domain and the membrane (Figure 6E). This orientation would prevent the access of the processing enzymes. By contrast, the N213 residue is fully accessible to the enzymes when CD38 is present as a dimer or a monomer. Accordingly, the high-mannose-type oligosaccharides of the N213 residue are indicative of the tetramerization of CD38 during the processing of the *N*-glycan.

## The Two Interaction Modes Are Crucial for the Catalytic Activity of CD38

Among the ADP-ribosyl cyclase family proteins, the catalytically important residues, W125, E146, W189, and E226 in human CD38, are located at spatially equivalent positions (Liu et al., 2005; Prasad et al., 1996; Yamamoto-Katayama et al., 2002). In the sequence, W125 and E146 are located near the α4 helix (boxed in Figure 2A). As shown in Figure 2H, the positions of W129 and E230 in the C-terminal-truncated extracellular domain of CD38 (shown in purple) were shifted by approximately 3 Å as compared to the corresponding residues, W125 and E226, in the full-length extracellular domain (shown in green). This displacement suggests the importance of the proper interaction between the C-terminal α9 helix and the α4 helix in catalytic-site formation, which is consistent with the

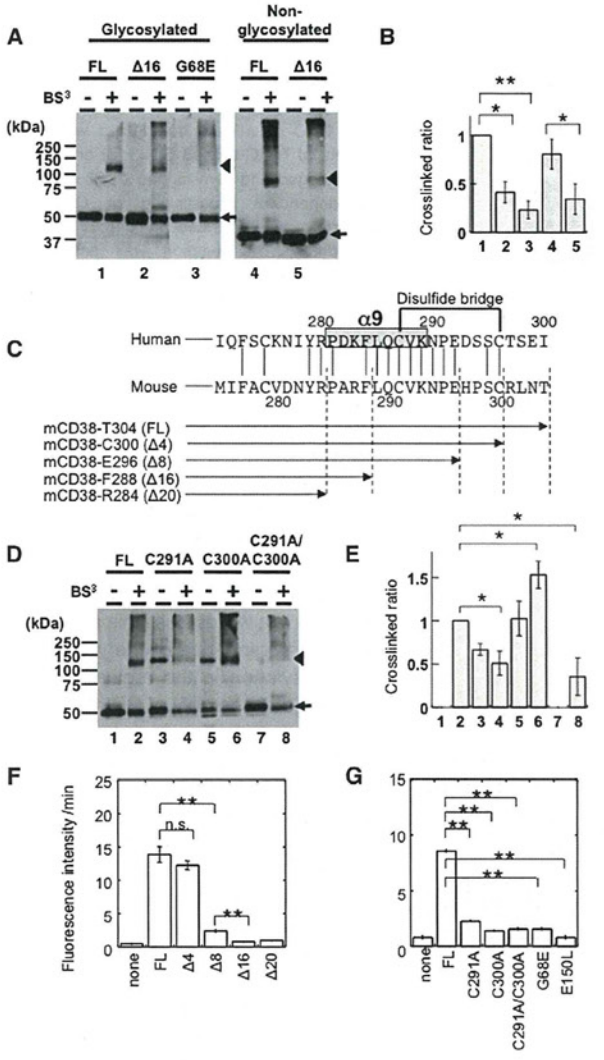


**Figure 4. The C-Terminal and Juxtamembrane α Helices Are Both Important for the Homophilic Interaction of CD38 on the Cell Surface and the Catalytic Activity**

(A and D) A20 cells ($1 \times 10^7$ cells/ml) transfected with glycosylated or non-glycosylated FLAG-tagged CD38 in either the FL or truncated form or with the indicated mutations were incubated in the absence or presence of $BS^3$. The proteins were detected by immunoblotting with a biotin-anti-FLAG pAb, as described in the Supplemental Experimental Procedures. The positions of the crosslinked dimers and the noncrosslinked monomers of CD38 are shown by triangles and arrows, respectively.

(B and E) The crosslinking ratios, which are the intensities of crosslinked dimer to noncrosslinked monomer in Figures 7A and 7D, respectively, are expressed as relative values to that without the truncation. Densitometric analysis was performed using the ImageJ software (http://rsbweb.nih.gov/ij/).

(C) Sequence alignment of the C-terminal regions of human and mouse CD38 and schematic representations of the FLAG-tagged mouse CD38 constructs to probe the roles of the C-terminal α-helix. The two conserved cysteine residues involved in the disulfide bridge (Cys287 and Cys296 in human CD38 and Cys291 and Cys300 in mouse CD38) are also shown.

(F and G) $NAD^+$ glycohydrolase activities of A20 cells (none) or CD38 transfectants without (FL) and with the C-terminal truncation or the mutations were measured. Significant differences are indicated: ** = $p < 0.01$; n.s. = not significant ($p > 0.05$). Values are means ± SD ($n = 3$). See also Figure S4.

results previously reported for calcium-loaded CD38 (Liu et al., 2008).

In the case of the isolated extracellular domain, both the C-terminal truncation of 16 amino acid residues and the G68E mutation appreciably decreased the $NAD^+$ glycohydrolase activity (Figure S4E). In addition, the $BS^3$-crosslinking and the specific activity of the $NAD^+$ glycohydrolase were decreased at a lower concentration of the extracellular domain (Figures S4F and S4G), implying that proper assembly is important for the catalytic activity of CD38 in solution.

In A20 cells, the C-terminal truncation of four amino acid residues did not affect the $NAD^+$ glycohydrolase activity of CD38 (Figure 4F), which is consistent with the fact that the four residues are disordered in the crystal structure of human CD38 (Liu et al., 2005). However, the truncation of eight amino acid residues appreciably reduced the $NAD^+$ glycohydrolase activity. This may be due to the loss of the disulfide bond between Cys291 and Cys300, which is conserved among the family proteins (Figure 4C), since the mutations affecting the disulfide bond appreciably reduced the catalytic activity (Figure 4G). The truncation of 16 and 20 amino acid residues resulted in the complete loss of the $NAD^+$ glycohydrolase activity. The cyclase activity was also diminished by the truncation of 16 amino acid residues (Figure S4D). Thus, the C-terminal region involving the type III interaction mode is crucial for the catalytic activity.

The G68E mutation in the α1 helix abolished the $NAD^+$ glycohydrolase activity of CD38 in A20 cells (Figure 4G). The effect was comparable to that of the mutation of the catalytically important Glu150 to Leu (E150L). A consistent result was previously obtained in Ba/F3 cells (Moreno-García et al., 2004). Since the G68E mutation disrupts the homophilic interaction (Figure 1 and Figure S1) and Gly68 participates in the type I interaction mode (Figure 3), it is suggested that the integrity of the type I interaction mode is necessary for the catalytic activity of CD38 on the cell surface. Accordingly, the two interaction modes are both crucial for the catalytic activity.

## The Two Interaction Modes Facilitate the Association of CD38 with Detergent-Resistant Membranes

Biochemical analyses have revealed the specific associations of several membrane proteins with detergent-resistant membranes (DRMs). DRMs are enriched in cholesterol and sphingolipids and can be isolated as low-density fractions from detergent-lysed cells (Brown and Rose, 1992). Although membrane rafts and DRMs should be carefully distinguished (Sonnino, 2008), DRMs can reflect important changes in the distribution of proteins on the membranes.

As shown in Figure 7A, CD38 was recovered in DRMs after A20 cells expressing CD38 were lysed with 1% Brij-58. The amounts of CD38 in DRMs were decreased by the G68E mutation in the α1 helix and by the C-terminal truncation (Figures 7B and 7C). We previously reported that the ligation of CD38 with the agonistic antimouse CD38 antibody, CS/2, increased the association of CD38 with DRMs in mouse splenic B cells (Hara-Yokoyama et al., 2008). The amount of wild-type CD38 in DRMs was further increased by treating A20 cells with CS/2. However, the amount of truncated CD38 in DRMs was not significantly increased by CS/2, although the C-terminal truncation did not reduce the binding of CS/2 to CD38 (Figure S6).

 

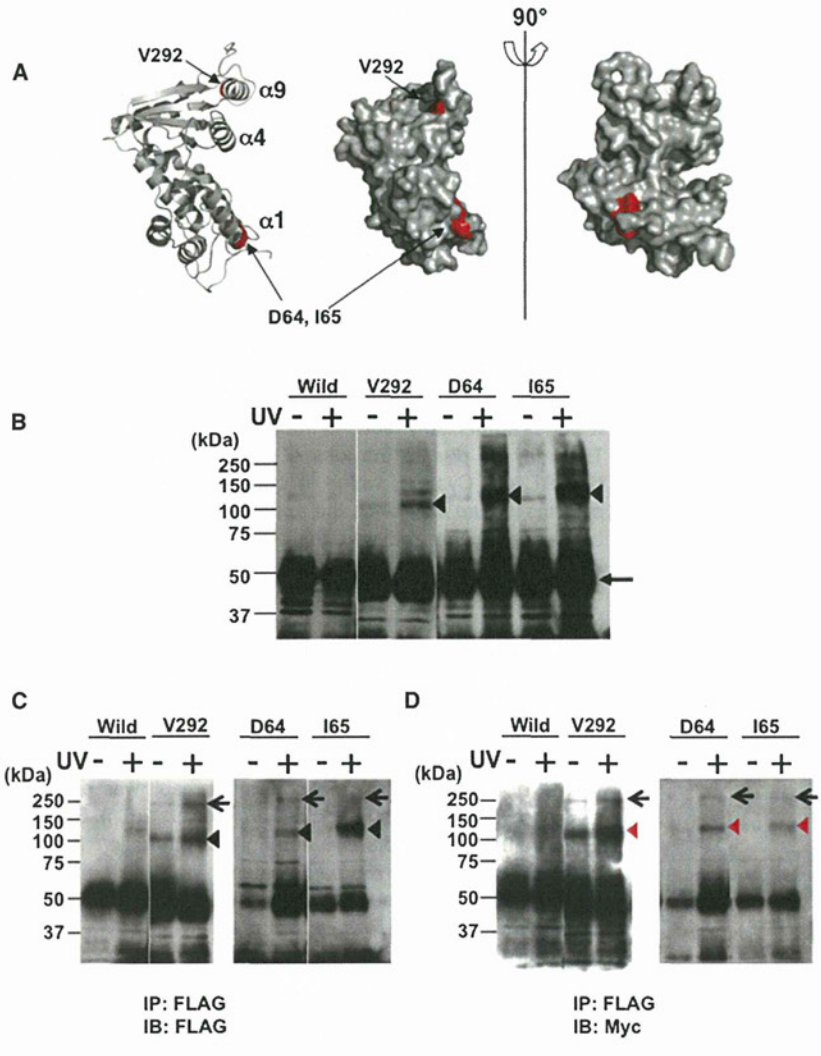


**Figure 5. Site-Specific Crosslinking of Cell-Surface CD38**

(A) The residues to which the crosslinker was introduced are shown in hCD38(R48-I300) in two perpendicular views.

(B–D) CHO cells were transfected with amber mutants of FLAG-tagged CD38 (B) or with both FLAG-tagged and Myc-tagged CD38 (C and D). Light-dependent crosslinking of CD38 was performed as described in the Experimental Procedures. The reaction was analyzed by immunoblotting with an anti-FLAG antibody (B and C) and an anti-Myc (D) antibody.

These results suggest that the two interaction modes contribute to the association of CD38 with DRMs.

In addition, we examined whether the C-terminal truncation affects the lipid composition of DRMs harboring CD38 (CD38-DRMs) by the immunoprecipitation of CD38 in DRMs. In this context, CD38 has an affinity for sphingolipids, as the catalytic activities of CD38 are inhibited by gangliosides (Hara-Yokoyama et al., 1996, 2001). In the CD38-DRMs, lipids were similarly detected with and without the C-terminal truncation, regardless of the CS/2 stimulation and glycosylation (Figure S6). Accordingly, it is unlikely that the C-terminal truncation alters the lipid composition in CD38-DRMs.

### Functional Aspects of N-Glycosylation of CD38

CD38 has four potential N-glycosylation sites (Gao and Mehta, 2007). We compared the wild-type and mutant CD38 proteins, in which the Asn residues were mutated to Asp residues (N104D/N124D/N213D/N223D), to evaluate the role of the *N*-glycosylation. Even in the absence of glycosylation, the C-terminal truncation reduced the $BS^3$-dependent crosslinking (Figures 4A and 4B) and abolished the catalytic activity (Figure S4). However, the truncation did not alter the amount of nonglycosylated CD38 in DRMs in both the presence and absence of CS/2 (Figures 7D and 7E). Thus, the glycosylated and nonglycosylated CD38 molecules associated with DRMs in different manners. We will discuss this point below from the perspective of the involvement of glycosylation in the regulation of the cell-surface assembly of CD38.

## DISCUSSION

In the present study, we demonstrated that the type I and type II/III interaction modes are involved in the assembly of mouse CD38 on the cell surface. The combination of the modes cooperatively stabilizes the tetramer. The type I interaction mode is primarily involved in the core homophilic interaction between the extracellular domains. The core dimer formed via the type I interaction mode is then assembled into the tetramer via the type II/III interaction mode, which provides a structural basis for the previously reported tetramerization. In the case of the extracellular domain, the association/dissociation in the dimer-tetramer equilibrium may be fast, and thus the tetramer was not detectable during analytical ultracentrifugation and size exclusion chromatography. Tetramerization occurs more efficiently with the full-length CD38 on the cell surface than the extracellular domain fragments in solution, probably because the orientation of the extracellular domain is restricted on the cell surface. Since the integrity of both interaction modes was required for the catalytic activity and the raft-association ability of CD38, we conclude that the tetramerization due to the dimer-of-dimers interaction is vital for the functional aspects of CD38 on the cell surface. Furthermore, we discovered the role of glycosylation in the regulation of the homophilic interaction of CD38. Thus, the assembly of CD38 is distinct from those of the other family members, although the structures of the protomers are well conserved among them, except for the orientation of the C-terminal α-helix (Liu et al., 2005).

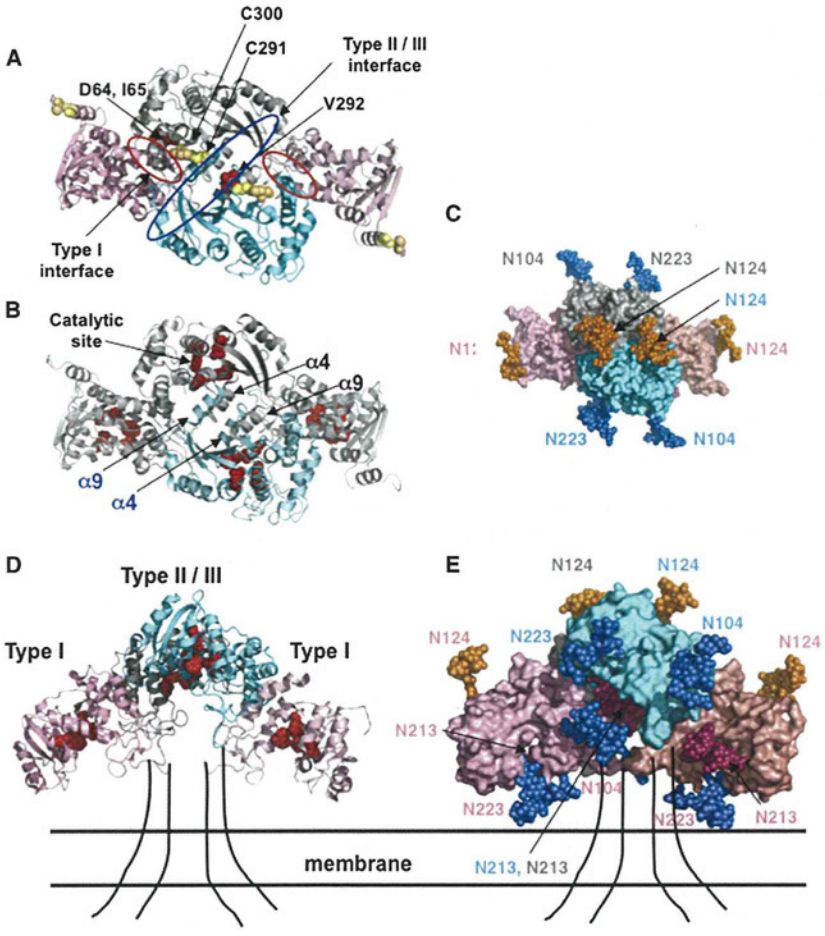


**Figure 6. Schematic Representations of the Dimer-of-Dimers Interactions of CD38 on the Cell Surface**

The four molecules of hCD38(R48-I300) are assembled by the type I interface (red oval) and by the type II/III interfaces (blue oval), as in mCD38mut(R48-F288) in the crystal (2EG9). The structures in (D and E) are shown in a perpendicular view to those in (A)–(C). The residues corresponding to D64, I65, and V292 of mouse CD38 are depicted in red, and those corresponding to C291 and C300 are yellow and light orange, respectively (A). The catalytically important residues (W125, E146, W189, and E226 in hCD38) are shown in red (B and D). (C and E) The structure of the *N*-linked oligosaccharide moiety from a fat-depleting factor (1ZAG), composed of nine sugar residues, is attached to the residues corresponding to the N-glycosylation sites of mouse CD38 (N104, N124, N213, and N223, respectively). See also Figure S5.

Within the tetramer of CD38, the α9 helix can interact with the α4 helix of the other CD38 molecule at the type III interface to reciprocally stabilize each other's active sites (Figure 6B). In this context, the pair of the α9 and α4 helices is considered to be a molecular device coupling the homophilic interaction to the catalytic site formation. The requirement of the type I interaction mode for the catalytic activity is explained by the stabilization of the type II/III interfaces via tetramerization.

A long-lasting topological problem is how the catalytic activity of the CD38 ectoenzyme is involved in intracellular calcium signaling (Malavasi et al., 2008). The oligomerized CD38 reportedly acts as a channel of cyclic ADP ribose (cADPR) (Franco et al., 1998). Intriguingly, in the tetramer structure, all of the catalytic sites face the space enclosed between the ectoenzyme and the membrane surface (Figure 6D). It would be tempting to determine whether the four transmembrane domains in the tetrameric assembly are the basis for the putative inward channel activity of the produced cADPR.

The clustering of membrane proteins enhances their targeting to membrane rafts (Hammond et al., 2005). The clustering of T cell receptors (TCR), B cell receptors (BCR), and FcεRI, caused by antigen/MHC complexes or oligomeric antigens, facilitates their recruitment to membrane rafts and triggers immune-recognition receptor signaling in T, B, and mast cells, respectively (Gupta and DeFranco, 2007; Jury et al., 2007; Silveira E Souza et al., 2011). The present study suggests that the raft-targeting of CD38 requires its intrinsic clustering on the cell surface rather than the lipid interaction. The C-terminal and juxtamembrane helices of CD38 are required, but the defect due to the C-terminal truncation is not compensated by the ligation with the agonistic antibody. Therefore, the integrity of the two modes of homophilic interactions enabling tetramerization appears to be essential. However, at present, we have not succeeded in detecting the CD38 tetramer clearly after SDS-PAGE. The tetramer is probably stabilized on the membrane and readily dissociates to monomers or dimers in the presence of detergent. A more sophisticated approach, such as single-molecule tracking on live cells, will be required to detect the tetrameric form on the cell surface. Additionally, no partner molecule within membrane rafts that can generally explain the raft-targeting of CD38 has been identified, although the association of CD38 with the Src family protein tyrosine kinase Lck has been reported (Cho et al., 2000). It is conceivable that the identification of the CD38 partner would require experimental conditions that maintain the integrity of the CD38 tetramer.

In contrast to the glycosylated CD38, the effect of the C-terminal truncation on the association of CD38 with DRMs was not observed in the absence of *N*-glycosylation. The absence of the *N*-glycans attached to N104 and N223 is considered to enable the formation of the "type IV" interface (Figure 3K). Actually, $BS^3$-dependent high-molecular mass aggregates of CD38 were observed in the absence of glycosylation. Similar results were obtained in HeLa and Michigan Cancer Foundation (MCF)-7 cells (Gao and Mehta, 2007). Thus, the *N*-glycans probably regulate the assembly of CD38 on the cell surface by inhibiting the "aggregating" type IV interface.

 

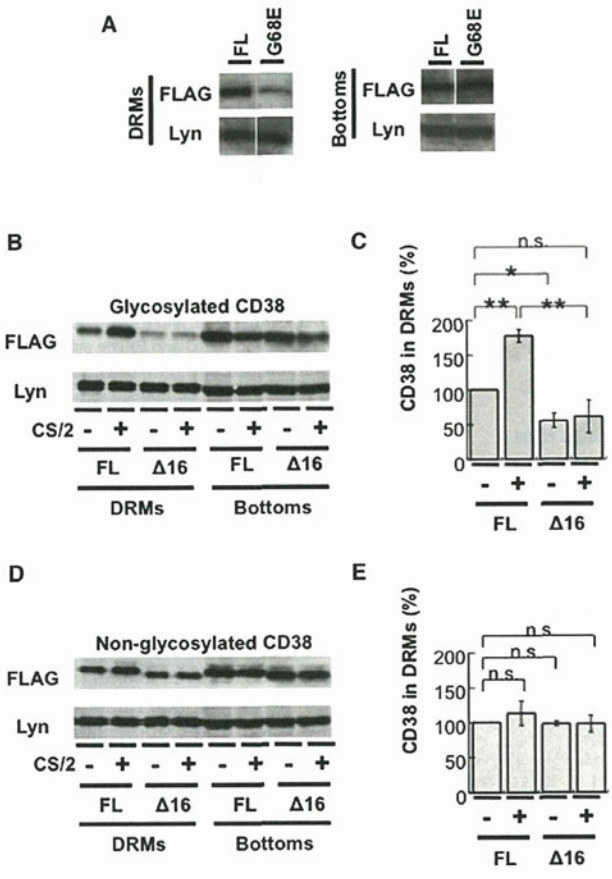


**Figure 7. The C-Terminal Region Truncation and the G68E Mutation Decrease the Association of Glycosylated CD38 with DRMs**

(A) A20 cells transfected with glycosylated FLAG-tagged CD38 ($2 \times 10^8$ cells/ml), without (FL) and with the G68E mutation, were lysed in 1% Brij-58 lysis buffer.

(B and D) A20 cells transfected with glycosylated (B) and nonglycosylated (D) FLAG-tagged CD38 ($2 \times 10^8$ cells/ml) in either the full-length (FL) or truncated form were stimulated with 20 μg/ml CS/2 and then lysed. Lysates were fractionated by sucrose density gradient ultracentrifugation, as described in the Supplemental Experimental Procedures. Proteins in the DRM and bottom fractions were separated by 10% SDS-PAGE and were detected by immunoblotting with a biotinylated anti-FLAG pAb and an anti-Lyn pAb. Essentially, the same results were obtained in an independent experiment.

(C and E) The intensities of the bands in (B and D) were quantified and expressed as the relative values to that without the truncation (FL) in the absence of CS/2. Densitometric analysis of the band intensity was performed using the ImageJ software. Values are means ± SD (n = 3). Significant differences are indicated: ** = $p < 0.01$; * = $p < 0.05$; n.s. = not significant ($p > 0.05$). See also Figure S6.

Recently, the mono *N*-glycosylated forms of bovine CD38 have been revealed as parallel "back-to-back" homodimers (Egea et al., 2012), which would not be allowed in the case of mouse CD38 due to the glycosylation at N124. Thus, the assembly of CD38 might have diversity among species.

From a clinical point of view, CD38 is recognized as a negative prognostic indicator in B cell chronic lymphocytic leukemia patients and in individuals infected with HIV (Malavasi et al., 2008). Based on studies using B cell chronic lymphocytic leukemia cells, CD38 is a potential signaling molecule that regulates cell fate rather than a mere marker (Malavasi et al., 2008). Autoantibodies against CD38 reportedly impaired glucose-induced insulin secretion in a noninsulin-dependent diabetes patient (Ikehata et al., 1998). Considering the functional importance of the cell-surface assembly of mouse CD38 demonstrated here, the assembly of human CD38 should be resolved to develop a new therapeutic strategy, in which the disassembly of CD38 can be manipulated.

## EXPERIMENTAL PROCEDURES

### Protein Expression and Purification

The extracellular domains of CD38 were transiently expressed as secreted proteins in *Drosophila* S2 cells and purified as described previously (Hara-Yokoyama et al., 2008). Plasmid construction is described in the Supplemental Experimental Procedures. For the crystallization, the four Asn residues were mutated to Asp residues (N104D, N124D, N213D, and N223D).

### Crystallization and Data Collection

The crystallization screening of FLAG-mCD38mut(R48-F288) was performed by the sitting-drop vapor diffusion method (protein at 7.4 mg/ml) at 20°C. Diffraction quality crystals were grown by the addition of 0.2 M NDSB-256 (Hampton Research) to the sitting drops, which were equilibrated against a reservoir solution containing 25% polyethylene glycol 1500 (PEG1500). The crystals belonged to the primitive orthorhombic space group $P2_12_12$, with unit cell constants of $a$ = 59.1 Å, $b$ = 176.8 Å, $c$ = 44.6 Å, and contained two CD38 molecules per asymmetric unit. Single crystals were coated with Paratone-N and 10% glycerol, mounted using a nylon loop (Hampton Research), and flash-cooled in the cold stream of the goniometer. The data were collected with a wavelength of 1.0 Å on beamline BL26B2 at SPring-8 (Harima, Japan) and were recorded on a Jupiter210 charge-coupled device detector (Rigaku). The diffraction data were processed with the HKL2000 program (Otwinowski and Minor, 1997).

### Structure Determination and Refinement

The structure of FLAG-mCD38mut(R48-F288) was determined by molecular replacement with the program MOLREP (CCP4), using human CD38 (PDBID: 2DF1) as the search model. The model was corrected iteratively using O (Jones et al., 1991), and structure refinement was performed using Crystallography and NMR system (Brünger et al., 1998). Refinement statistics are presented in Table 1. The quality of the model was inspected by the program PROCHECK (Laskowski et al., 1993). Graphic figures were created using the program PyMOL (http://www.pymol.org). The atomic coordinates have been deposited in the Protein Data Bank, with the accession code 2EG9.

### Cells

The murine B lymphoma-derived cell line A20 and the CHO cells were maintained in Roswell Park Memorial Institute 1640 medium supplemented with 8% fetal bovine serum and 50 μM 2-mercaptoethanol and in minimum essential medium supplemented with 10% fetal bovine serum, respectively. Both media contained penicillin and streptomycin.

### Stable Transfectants

Plasmid construction is described in the Supplemental Experimental Procedures. Transfection of A20 cells was performed using the Nucleofector technology (Amaxa), and puromycin-resistant cells were obtained.

### Site-Specific Crosslinking

The CD38 gene in pCEpuro-mCD38-T304 was mutagenized to create an amber codon located at H61, D64, I65, L67, R69, L71, L77, L135, L137, T140, W141, I142, P285, or V292. Each amber mutant CD38 gene (5 μg DNA) was cotransfected into CHO cells ($5 \times 10^6$ cells) with pcpBpaRS ver.1 (5 μg DNA), carrying the bacterial pair of an amber suppressor transfer RNA (tRNA) and an aminoacyl-tRNA synthetase specific to *p*-benzoyl-L-phenylalanine (*p*Bpa) (Hino et al., 2005, 2006), using Lipofectamine 2000 (36 μl). Among

the mutants, the protein was sufficiently expressed in the presence of *p*Bpa when the amber codon was introduced at positions D64, I65, and V292 after overnight culture. The cells were then exposed to UV light and lysed with 1% Triton X-100 in buffer A, consisting of 20 mM Tris-HCl, 150 mM NaCl, 10 mM iodoacetamide, 2.5 mM NaF, 2.5 mM sodium pyrophosphate, 10 mM ethylenediaminetetraacetic acid, 10 mM β-glycerophosphate, 1 mM sodium orthovanadate, 1 mM phenylmethylsulfonyl fluoride, 5 μg/ml leupeptin, 10 μg/ml pepstatin, and 10 μg/ml aprotinin, pH 7.5. Cell lysates were incubated for 2 hr at 4°C with a 10 μl slurry of anti-FLAG M2 agarose resin. After the resin was washed, the complexes were eluted with 100 μg/ml FLAGx3 peptide and analyzed by immunoblotting.

### Statistical Analysis

Differences between mean values were assessed by the Student's t test. The statistical significance was set at P less than .01 or .05.

## SUPPLEMENTAL INFORMATION

Supplemental Information includes six figures and Supplemental Experimental Procedures and can be found with this article online at http://dx.doi.org/10.1016/j.str.2012.06.017.

## ACKNOWLEDGMENTS

We thank Mio Inoue, Tomomi Uchikubo-Kamo, and Seisuke Kusano (RIKEN Systems and Structural Biology Center) for the preparation of CD38 proteins, Prof. Chan Fong Chang (National University of Singapore) for valuable discussions, and Prof. Hidetoshi Kobayashi (RIKEN) for providing lysenin and the anti-lysenin antibody. This work was supported by the Targeted Proteins Research Program (TPRP) and Grants-in-Aid for Scientific Research 22592060 (to M.H.), 23650319 (to K.A.P.), and 23659108 (to M.Y.), as well as grants from the Global Center of Excellence (GCOE) Program from the Ministry of Education, Culture, Sports, Science, and Technology, Japan.

Received: January 16, 2012
Revised: June 22, 2012
Accepted: June 30, 2012
Published online: August 2, 2012

## REFERENCES

Aksoy, P., Escande, C., White, T.A., Thompson, M., Soares, S., Benech, J.C., and Chini, E.N. (2006). Regulation of SIRT 1 mediated NAD dependent deacetylation: a novel role for the multifunctional enzyme CD38. Biochem. Biophys. Res. Commun. *349*, 353–359.

Brown, D.A., and Rose, J.K. (1992). Sorting of GPI-anchored proteins to glycolipid-enriched membrane subdomains during transport to the apical cell surface. Cell *68*, 533–544.

Brünger, A.T., Adams, P.D., Clore, G.M., DeLano, W.L., Gros, P., Grosse-Kunstleve, R.W., Jiang, J.S., Kuszewski, J., Nilges, M., Pannu, N.S., et al. (1998). Crystallography & NMR system: A new software suite for macromolecular structure determination. Acta Crystallogr. D Biol. Crystallogr. *54*, 905–921.

Bruzzone, S., Guida, L., Franco, L., Zocchi, E., Corte, G., and De Flora, A. (1998). Dimeric and tetrameric forms of catalytically active transmembrane CD38 in transfected HeLa cells. FEBS Lett. *433*, 275–278.

Chidambaram, N., Wong, E.T., and Chang, C.F. (1998). Differential oligomerization of membrane-bound CD38/ADP-ribosyl cyclase in porcine heart microsomes. Biochem. Mol. Biol. Int. *44*, 1225–1233.

Cho, Y.S., Han, M.K., Choi, Y.B., Yun, Y., Shin, J., and Kim, U.H. (2000). Direct interaction of the CD38 cytoplasmic tail and the Lck SH2 domain. Cd38 transduces T cell activation signals through associated Lck. J. Biol. Chem. *275*, 1685–1690.

Cockayne, D.A., Muchamuel, T., Grimaldi, J.C., Muller-Steffner, H., Randall, T.D., Lund, F.E., Murray, R., Schuber, F., and Howard, M.C. (1998). Mice deficient for the ecto-nicotinamide adenine dinucleotide glycohydrolase CD38 exhibit altered humoral immune responses. Blood *92*, 1324–1333.

Deaglio, S., Zubiaur, M., Gregorini, A., Bottarel, F., Ausiello, C.M., Dianzani, U., Sancho, J., and Malavasi, F. (2002). Human CD38 and CD16 are functionally dependent and physically associated in natural killer cells. Blood *99*, 2490–2498.

Deaglio, S., Capobianco, A., Bergui, L., Dürig, J., Morabito, F., Dührsen, U., and Malavasi, F. (2003). CD38 is a signaling molecule in B-cell chronic lymphocytic leukemia cells. Blood *102*, 2146–2155.

Deaglio, S., Vaisitti, T., Billington, R., Bergui, L., Omede', P., Genazzani, A.A., and Malavasi, F. (2007). CD38/CD19: a lipid raft-dependent signaling complex in human B cells. Blood *109*, 5390–5398.

Egea, P.F., Muller-Steffner, H., Kuhn, I., Cakir-Kiefer, C., Oppenheimer, N.J., Stroud, R.M., Kellenberger, E., and Schuber, F. (2012). Insights into the mechanism of bovine CD38/NAD+glycohydrolase from the X-ray structures of its michaelis complex and covalently-trapped intermediates. PLoS ONE *7*, e34918.

Franco, L., Guida, L., Bruzzone, S., Zocchi, E., Usai, C., and De Flora, A. (1998). The transmembrane glycoprotein CD38 is a catalytically active transporter responsible for generation and influx of the second messenger cyclic ADP-ribose across membranes. FASEB J. *12*, 1507–1520.

Frasca, L., Fedele, G., Deaglio, S., Capuano, C., Palazzo, R., Vaisitti, T., Malavasi, F., and Ausiello, C.M. (2006). CD38 orchestrates migration, survival, and Th1 immune response of human mature dendritic cells. Blood *107*, 2392–2399.

Fukushi, Y., Kato, I., Takasawa, S., Sasaki, T., Ong, B.H., Sato, M., Ohsaga, A., Sato, K., Shirato, K., Okamoto, H., and Maruyama, Y. (2001). Identification of cyclic ADP-ribose-dependent mechanisms in pancreatic muscarinic Ca(2+) signaling using CD38 knockout mice. J. Biol. Chem. *276*, 649–655.

Gao, Y., and Mehta, K. (2007). N-linked glycosylation of CD38 is required for its structure stabilization but not for membrane localization. Mol. Cell. Biochem. *295*, 1–7.

Gelman, L., Deterre, P., Gouy, H., Boumsell, L., Debré, P., and Bismuth, G. (1993). The lymphocyte surface antigen CD38 acts as a nicotinamide adenine dinucleotide glycohydrolase in human T lymphocytes. Eur. J. Immunol. *23*, 3361–3364.

Gupta, N., and DeFranco, A.L. (2007). Lipid rafts and B cell signaling. Semin. Cell Dev. Biol. *18*, 616–626.

Hammond, A.T., Heberle, F.A., Baumgart, T., Holowka, D., Baird, B., and Feigenson, G.W. (2005). Crosslinking a lipid raft component triggers liquid ordered-liquid disordered phase separation in model plasma membranes. Proc. Natl. Acad. Sci. USA *102*, 6320–6325.

Hara-Yokoyama, M., Kukimoto, I., Nishina, H., Kontani, K., Hirabayashi, Y., Irie, F., Sugiya, H., Furuyama, S., and Katada, T. (1996). Inhibition of NAD+ glycohydrolase and ADP-ribosyl cyclase activities of leukocyte cell surface antigen CD38 by gangliosides. J. Biol. Chem. *271*, 12951–12955.

Hara-Yokoyama, M., Nagatsuka, Y., Katsumata, O., Irie, F., Kontani, K., Hoshino, S., Katada, T., Ono, Y., Fujita-Yoshigaki, J., Sugiya, H., et al. (2001). Complex gangliosides as cell surface inhibitors for the ecto-NAD+ glycohydrolase of CD38. Biochemistry *40*, 888–895.

Hara-Yokoyama, M., Kimura, T., Kaku, H., Wakiyama, M., Kaitsu, Y., Inoue, M., Kusano, S., Shirouzu, M., Yokoyama, S., Katada, T., et al. (2008). Alteration of enzymatic properties of cell-surface antigen CD38 by agonistic anti-CD38 antibodies that prolong B cell survival and induce activation. Int. Immunopharmacol. *8*, 59–70.

Hino, N., Okazaki, Y., Kobayashi, T., Hayashi, A., Sakamoto, K., and Yokoyama, S. (2005). Protein photo-cross-linking in mammalian cells by site-specific incorporation of a photoreactive amino acid. Nat. Methods *2*, 201–206.

Hino, N., Hayashi, A., Sakamoto, K., and Yokoyama, S. (2006). Site-specific incorporation of non-natural amino acids into proteins in mammalian cells with an expanded genetic code. Nat. Protoc. *1*, 2957–2962.

Ikehata, F., Satoh, J., Nata, K., Tohgo, A., Nakazawa, T., Kato, I., Kobayashi, S., Akiyama, T., Takasawa, S., Toyota, T., and Okamoto, H. (1998). Autoantibodies against CD38 (ADP-ribosyl cyclase/cyclic ADP-ribose

 

hydrolase) that impair glucose-induced insulin secretion in noninsulin- dependent diabetes patients. J. Clin. Invest. *102*, 395–401.

Jackson, D.G., and Bell, J.I. (1990). Isolation of a cDNA encoding the human CD38 (T10) molecule, a cell surface glycoprotein with an unusual discontinuous pattern of expression during lymphocyte differentiation. J. Immunol. *144*, 2811–2815.

Jin, D., Liu, H.X., Hirai, H., Torashima, T., Nagai, T., Lopatina, O., Shnayder, N.A., Yamada, K., Noda, M., Seike, T., et al. (2007). CD38 is critical for social behaviour by regulating oxytocin secretion. Nature *446*, 41–45.

Jones, T.A., Zou, J.Y., Cowan, S.W., and Kjeldgaard, M. (1991). Improved methods for building protein models in electron density maps and the location of errors in these models. Acta Crystallogr. A *47*, 110–119.

Jury, E.C., Flores-Borja, F., and Kabouridis, P.S. (2007). Lipid rafts in T cell signalling and disease. Semin. Cell Dev. Biol. *18*, 608–615.

Kato, I., Yamamoto, Y., Fujimura, M., Noguchi, N., Takasawa, S., and Okamoto, H. (1999). CD38 disruption impairs glucose-induced increases in cyclic ADP-ribose, [Ca2+]i, and insulin secretion. J. Biol. Chem. *274*, 1869–1872.

Kato, K., and Kamiya, Y. (2007). Structural views of glycoprotein-fate determination in cells. Glycobiology *17*, 1031–1044.

Kontani, K., Nishina, H., Ohoka, Y., Takahashi, K., and Katada, T. (1993). NAD glycohydrolase specifically induced by retinoic acid in human leukemic HL-60 cells. Identification of the NAD glycohydrolase as leukocyte cell surface antigen CD38. J. Biol. Chem. *268*, 16895–16898.

Laskowski, R.A., MacArthur, M.W., Moss, D.S., and Thornton, J.M. (1993). PROCHECK: a program to check the stereochemical quality of protein structures. J. Appl. Cryst. *26*, 283–291.

Lee, H.C. (1994). Cyclic ADP-ribose: a calcium mobilizing metabolite of NAD+. Mol. Cell. Biochem. *138*, 229–235.

Lee, H.C. (2005). Nicotinic acid adenine dinucleotide phosphate (NAADP)-mediated calcium signaling. J. Biol. Chem. *280*, 33693–33696.

Liu, Q., Kriksunov, I.A., Graeff, R., Munshi, C., Lee, H.C., and Hao, Q. (2005). Crystal structure of human CD38 extracellular domain. Structure *13*, 1331–1339.

Liu, Q., Graeff, R., Kriksunov, I.A., Lam, C.M., Lee, H.C., and Hao, Q. (2008). Conformational closure of the catalytic site of human CD38 induced by calcium. Biochemistry *47*, 13966–13973.

Lund, F.E., Muller-Steffner, H.M., Yu, N., Stout, C.D., Schuber, F., and Howard, M.C. (1999). CD38 signaling in B lymphocytes is controlled by its ectodomain but occurs independently of enzymatically generated ADP-ribose or cyclic ADP-ribose. J. Immunol. *162*, 2693–2702.

Lund, F.E., Muller-Steffner, H., Romero-Ramirez, H., Moreno-García, M.E., Partida-Sánchez, S., Makris, M., Oppenheimer, N.J., Santos-Argumedo, L., and Schuber, F. (2006). CD38 induces apoptosis of a murine pro-B leukemic cell line by a tyrosine kinase-dependent but ADP-ribosyl cyclase- and NAD glycohydrolase-independent mechanism. Int. Immunol. *18*, 1029–1042.

Malavasi, F., Deaglio, S., Funaro, A., Ferrero, E., Horenstein, A.L., Ortolan, E., Vaisitti, T., and Aydin, S. (2008). Evolution and function of the ADP ribosyl cyclase/CD38 gene family in physiology and pathology. Physiol. Rev. *88*, 841–886.

Mallone, R., Ferrua, S., Morra, M., Zocchi, E., Mehta, K., Notarangelo, L.D., and Malavasi, F. (1998). Characterization of a CD38-like 78-kilodalton soluble protein released from B cell lines derived from patients with X-linked agammaglobulinemia. J. Clin. Invest. *101*, 2821–2830.

Manjarrez-Orduño, N., Moreno-García, M.E., Fink, K., and Santos-Argumedo, L. (2007). CD38 cross-linking enhances TLR-induced B cell proliferation but decreases IgM plasma cell differentiation. Eur. J. Immunol. *37*, 358–367.

Moreno-García, M.E., Partida-Sánchez, S., Primack, J., Sumoza-Toledo, A., Muller-Steffner, H., Schuber, F., Oppenheimer, N., Lund, F.E., and Santos-Argumedo, L. (2004). CD38 is expressed as noncovalently associated homodimers on the surface of murine B lymphocytes. Eur. J. Biochem. *271*, 1025–1034.

Muñoz, P., Mittelbrunn, M., de la Fuente, H., Pérez-Martínez, M., García-Pérez, A., Ariza-Veguillas, A., Malavasi, F., Zubiaur, M., Sánchez-Madrid, F., and Sancho, J. (2008). Antigen-induced clustering of surface CD38 and recruitment of intracellular CD38 to the immunologic synapse. Blood *111*, 3653–3664.

Munshi, C., Baumann, C., Levitt, D., Bloomfield, V.A., and Lee, H.C. (1998). The homo-dimeric form of ADP-ribosyl cyclase in solution. Biochim. Biophys. Acta *1388*, 428–436.

Otwinowski, Z., and Minor, W. (1997). Processing of X-ray diffraction data collected in oscillation mode. Methods Enzymol. *276*, 307–326.

Partida-Sánchez, S., Cockayne, D.A., Monard, S., Jacobson, E.L., Oppenheimer, N., Garvy, B., Kusser, K., Goodrich, S., Howard, M., Harmsen, A., et al. (2001). Cyclic ADP-ribose production by CD38 regulates intracellular calcium release, extracellular calcium influx and chemotaxis in neutrophils and is required for bacterial clearance in vivo. Nat. Med. *7*, 1209–1216.

Partida-Sánchez, S., Goodrich, S., Kusser, K., Oppenheimer, N., Randall, T.D., and Lund, F.E. (2004). Regulation of dendritic cell trafficking by the ADP-ribosyl cyclase CD38: impact on the development of humoral immunity. Immunity *20*, 279–291.

Prasad, G.S., McRee, D.E., Stura, E.A., Levitt, D.G., Lee, H.C., and Stout, C.D. (1996). Crystal structure of Aplysia ADP ribosyl cyclase, a homologue of the bifunctional ectozyme CD38. Nat. Struct. Biol. *3*, 957–964.

Sato, A., Yamamoto, S., Kajimura, N., Oda, M., Usukura, J., and Jingami, H. (1999). Inhibitor peptide SNP-1 binds to a soluble form of BST-1/CD157 at a 2:2 stoichiometry. Eur. J. Biochem. *264*, 439–445.

Silveira E Souza, A.M., Mazucato, V.M., Jamur, M.C., and Oliver, C. (2011). Lipid rafts in mast cell biology. J. Lipids *2011*, 752906.

Sonnino, S.A.P. (2008). Membrane lipid domains and membrane lipid domain preparations: are they the same thing? Trends Glycosci. Glycotechnol. *20*, 315–340.

Takasawa, S., Nata, K., Yonekura, H., and Okamoto, H. (1993). Cyclic ADP-ribose in insulin secretion from pancreatic beta cells. Science *259*, 370–373.

Umar, S., Malavasi, F., and Mehta, K. (1996). Post-translational modification of CD38 protein into a high molecular weight form alters its catalytic properties. J. Biol. Chem. *271*, 15922–15927.

Yamamoto-Katayama, S., Ariyoshi, M., Ishihara, K., Hirano, T., Jingami, H., and Morikawa, K. (2002). Crystallographic studies on human BST-1/CD157 with ADP-ribosyl cyclase and NAD glycohydrolase activities. J. Mol. Biol. *316*, 711–723.

Zilber, M.T., Setterblad, N., Vasselon, T., Doliger, C., Charron, D., Mooney, N., and Gelin, C. (2005). MHC class II/CD38/CD9: a lipid-raft-dependent signaling complex in human monocytes. Blood *106*, 3074–3081.

Zubiaur, M., Izquierdo, M., Terhorst, C., Malavasi, F., and Sancho, J. (1997). CD38 ligation results in activation of the Raf-1/mitogen-activated protein kinase and the CD3-zeta/zeta-associated protein-70 signaling pathways in Jurkat T lymphocytes. J. Immunol. *159*, 193–205.

LETTER

doi:10.1038/nature11778

# Rotation mechanism of *Enterococcus hirae* $V_1$-ATPase based on asymmetric crystal structures

Satoshi Arai[1,2]*, Shinya Saijo[2,3]*, Kano Suzuki[1]*, Kenji Mizutani[1,2,4], Yoshimi Kakinuma[5], Yoshiko Ishizuka-Katsura[6], Noboru Ohsawa[6], Takaho Terada[6], Mikako Shirouzu[6], Shigeyuki Yokoyama[6,7,8], So Iwata[4,6], Ichiro Yamato[2] & Takeshi Murata[1,6,9]

**In various cellular membrane systems, vacuolar ATPases (V-ATPases) function as proton pumps, which are involved in many processes such as bone resorption and cancer metastasis, and these membrane proteins represent attractive drug targets for osteoporosis and cancer[1]. The hydrophilic $V_1$ portion is known as a rotary motor, in which a central axis DF complex rotates inside a hexagonally arranged catalytic $A_3B_3$ complex using ATP hydrolysis energy, but the molecular mechanism is not well defined owing to a lack of high-resolution structural information. We previously reported on the *in vitro* expression, purification and reconstitution of *Enterococcus hirae* $V_1$-ATPase from the $A_3B_3$ and DF complexes[2,3]. Here we report the asymmetric structures of the nucleotide-free (2.8 Å) and nucleotide-bound (3.4 Å) $A_3B_3$ complex that demonstrate conformational changes induced by nucleotide binding, suggesting a binding order in the right-handed rotational orientation in a cooperative manner. The crystal structures of the nucleotide-free (2.2 Å) and nucleotide-bound (2.7 Å) $V_1$-ATPase are also reported. The more tightly packed nucleotide-binding site seems to be induced by DF binding, and ATP hydrolysis seems to be stimulated by the approach of a conserved arginine residue. To our knowledge, these asymmetric structures represent the first high-resolution view of the rotational mechanism of $V_1$-ATPase.**

V-ATPases are thought to have originated from an ancestral enzyme in common with F-ATPases, which function as ATP synthases in mitochondria, chloroplasts and oxidative bacteria[4,5]. These ATPases possess an overall similar structure that is composed of a hydrophilic domain ($V_1$ and $F_1$) and a membrane-embedded ion-transporting domain ($V_o$ and $F_o$), and they have a similar reaction mechanism that occurs through rotation[1]. The rotational catalysis of $F_1$-ATPase has been investigated in detail, and the molecular mechanism has been proposed on the basis of crystal structures of the complex from bovine[6–9], yeast[10–12] and bacteria[13,14], and extensive single-molecule observation of the rotation[15–17]. Similar $V_1$-ATPase experiments have been conducted using the *Thermus thermophilus* enzyme, which functions physiologically as an ATP synthase[18]. The crystal structures of the $A_3B_3$ complex at 2.8 Å resolution[19] and the $A_3B_3$DF ($V_1$) complex at low resolution (4.5–4.8 Å)[20] suggest differences in its structure and interactions compared to $F_1$-ATPases. Single-molecule analyses of $V_1$-ATPase also suggest differences in torque generation and the coupling scheme of the rotation mechanism as compared to $F_1$ (ref. 21).

*Enterococcus hirae* V-ATPase, which acts as a primary ion pump similar to eukaryotic V-ATPases, uniquely transports $Na^+$ or $Li^+$ instead of $H^+$ ions[22–25]. The enzyme is composed of nine subunits with amino acid sequences that are homologous to those of the corresponding subunits of eukaryotic V-ATPases[26–28] (Supplementary Fig. 1). In this study, we solved the first asymmetric structures of $A_3B_3$ and $A_3B_3$DF ($V_1$) complexes at high resolution, which enabled the generation of a new model of the rotational mechanism.

The *E. hirae* $A_3B_3$ complex was purified and crystallized in the absence of nucleotide. The crystal structure was solved at a resolution of 2.8 Å (Supplementary Table 1). The three catalytic A subunits (Eh-A) and the three non-catalytic B subunits (Eh-B) are alternatively arranged and form a hexagonal ring (Fig. 1a). The structures of these subunits comprise the amino-terminal β-barrel domain, the central α/β domain and the carboxy-terminal helical domain (Supplementary Figs 2 and 3). The three Eh-A or Eh-B subunits in the $A_3B_3$ complex were shown to have similar secondary structures, but their three-dimensional conformations slightly differed (see Supplementary Fig. 4). We superimposed the N-terminal β-barrel region of the three Eh-A or Eh-B subunits to examine the conformational differences in the $A_3B_3$ complex, because this β-barrel domain should be fixed to form an alternatively arranged ring. One of the three Eh-A subunits adopts a closed conformation (denoted as $A_C$), which shifts the structure into the centre of the $A_3B_3$ ring, whereas the other two Eh-A subunits adopt similar open conformations (denoted as $A_O$ and $A_{O'}$), even though an α-helix (residues 261–275; designated as the 'arm') of the three Eh-A conformations was almost fixed (Fig. 1b and Supplementary Fig. 4). Similarly, one of the three Eh-B subunits shows a closed conformation (denoted as $B_C$) compared to the others (denoted as $B_O$ and $B_{O'}$) (Fig. 1c). Thus, the $A_3B_3$ hexamer assembled asymmetrically by adjacent $A_O$ and $B_O$, $A_{O'}$ and $B_{O'}$ and $A_C$ and $B_C$ subunits, whereas the conserved nucleotide-binding sites were located between the three different combinations: $A_OB_C$, $A_{O'}B_O$ and $A_CB_{O'}$ pairs (Fig. 1d).

The nucleotide-binding sites, which are comprised of the phosphate-binding loop (P-loop: GXXXXGKT(S)), the N-terminal portion of the arm (Glu 261 and Arg 262) in Eh-A, and Arg 350 (the 'Arg-finger' in ATPases) in Eh-B, had three different conformations (Fig. 1i–k). Electron density for nucleotides in the three binding sites was not observed (Supplementary Fig. 5), consistent with the absence of nucleotide contamination (ADP and ATP) detected in our sample and nucleotide-free crystallization conditions. Thus, surprisingly, the $A_3B_3$ complex, which is formed by three identical Eh-A and Eh-B subunits, demonstrated complete asymmetry without nucleotide binding (see Supplementary Fig. 6 for comparison with the symmetric structures of corresponding previously reported complexes of V- and F-ATPases). The observed asymmetric structure of nucleotide-free $A_3B_3$ (designated as $eA_3B_3$) may provide new insights for understanding the cooperative nature of the rotary motor as described below.

Next, we crystallized the $A_3B_3$ complex in the presence of a high concentration (5 mM) of the non-hydrolysable ATP analogue adenosine 5′-(β,γ-imino)triphosphate (AMP-PNP) with $MgSO_4$, and solved the structure of nucleotide-bound $A_3B_3$ (denoted as $bA_3B_3$) at

[1]Department of Chemistry, Graduate School of Science, Chiba University, 1-33 Yayoi-cho, Inage, Chiba 263-8522, Japan. [2]Department of Biological Science and Technology, Tokyo University of Science, 2641 Yamazaki, Noda-shi, Chiba 278-8510, Japan. [3]RIKEN SPring-8 Center, 1-1-1 Kouto, Sayo, Hyogo 679-5148, Japan. [4]Department of Cell Biology, Faculty of Medicine, Kyoto University, Yoshidakonoe-cho, Sakyo-ku, Kyoto 606-8501, Japan. [5]Laboratory of Molecular Physiology and Genetics, Faculty of Agriculture, Ehime University, 3-5-7 Tarumi, Matsuyama, Ehime 790-8566, Japan. [6]RIKEN Systems and Structural Biology Center, 1-7-22 Suehiro-cho, Tsurumi, Yokohama 230-0045, Japan. [7]Department of Biophysics and Biochemistry, Graduate School of Science, The University of Tokyo, 7-3-1 Hongo, Bunkyo-ku, Tokyo 113-0033, Japan. [8]Laboratory of Structural Biology, Graduate School of Science, The University of Tokyo, 7-3-1 Hongo, Bunkyo-ku, Tokyo 113-0033, Japan. [9]JST, PRESTO, 1-33 Yayoi-cho, Inage, Chiba 263-8522, Japan.

*These authors contributed equally to this work.

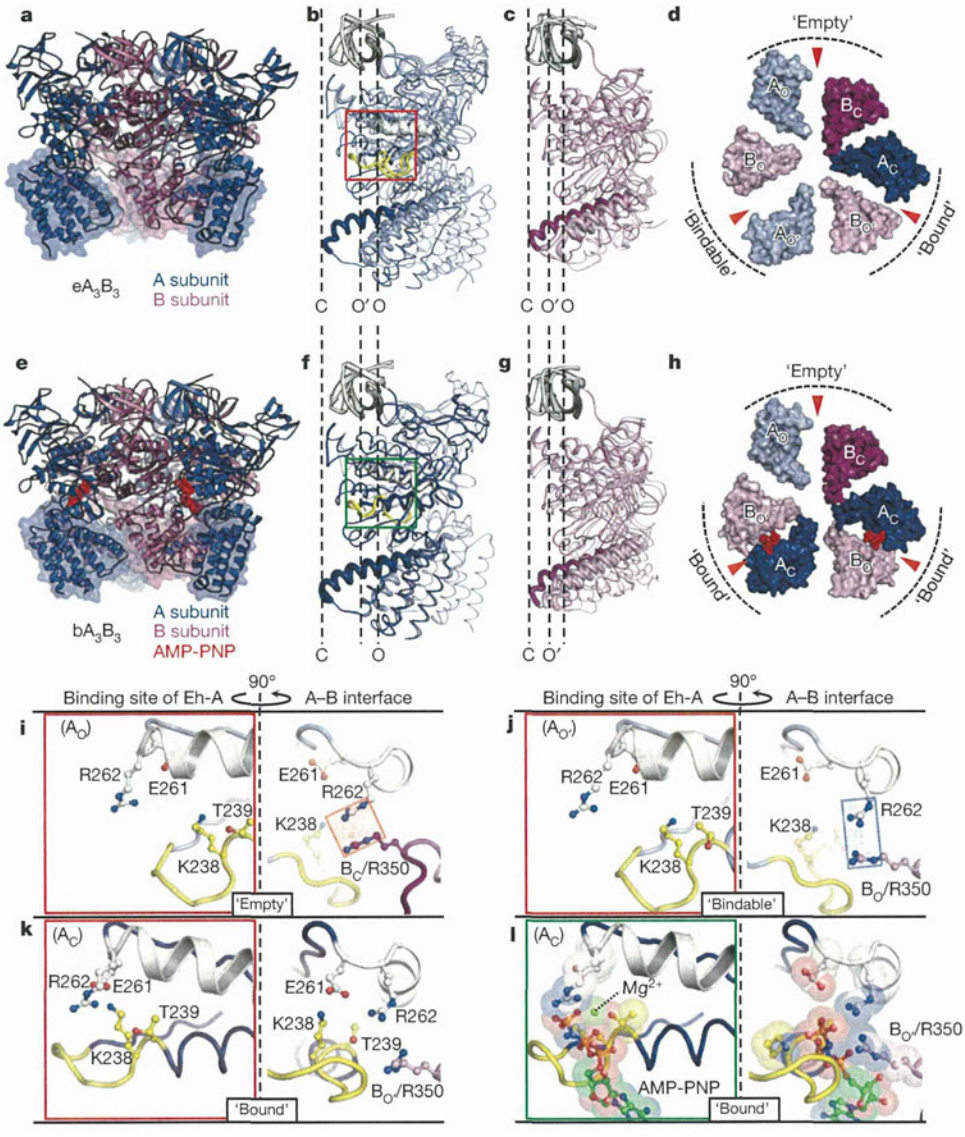


**Figure 1 | Structure of the $A_3B_3$ complex.** **a**, Side view of the nucleotide-free $A_3B_3$ structure ($eA_3B_3$). **b**, **c**, Superimposed structures at the N-terminal β-barrel (white) of three structures of Eh-A (**b**) and Eh-B (**c**) in $eA_3B_3$. Open (O and O') and closed (C) conformations of Eh-A and Eh-B are shown in light and dark colours, respectively. The P-loop and arm are shown in yellow and white, respectively. **d**, Top view of the C-terminal domain (shown in **a** as transparent surface) of $eA_3B_3$ from the N-terminal β-barrel side. Red arrows indicate the nucleotide-binding sites. **e**–**h**, Structures of the AMP-PNP-bound $A_3B_3$ complex ($bA_3B_3$) viewed and coloured as in **a**–**d**. **i**–**l**, Magnified nucleotide-binding sites with conserved residues, corresponding to red (**b**) and green (**f**) boxes. Right panels show the A–B interfaces rotated 90° around a vertical axis from the left panels.

a resolution of 3.4 Å (Supplementary Table 1). Two strong electron density peaks for AMP-PNP:Mg were found at the nucleotide-binding pockets in two Eh-AB pairs (Supplementary Fig. 7). The other AB pair, in which no density for nucleotide was found, was very similar to the $A_OB_C$ pair in $eA_3B_3$ (root mean squared deviation (r.m.s.d.) = 0.477 Å). We designated these $A_OB_C$ pairs as the 'empty' form on the basis of their apparent very low affinity for AMP-PNP:Mg. The two AMP-PNP:Mg-bound AB pairs were very similar to each other (r.m.s.d. = 0.511 Å), and were also similar to the $A_CB_{O'}$ pair in $eA_3B_3$ (r.m.s.d. = 0.683 Å and 0.719 Å) except for the side-chain conformations that directly interacted with AMP-PNP:Mg (Fig. 1k, l and Supplementary Fig. 8). This finding suggests that the $A_CB_{O'}$ pair of $eA_3B_3$ takes the ATP-bound form even in the absence of nucleotide; we designated these $A_CB_{O'}$ pairs as the 'bound' form. Furthermore, the more open $A_{O'}B_O$ pair of $eA_3B_3$ seemed to bind AMP-PNP:Mg and to change to the bound form of $bA_3B_3$; that is, binding of AMP-PNP:Mg induced the conformational change of $A_3B_3$ from the $A_{O'}B_O$ pair to the $A_CB_{O'}$ pair (see Supplementary Video 1). We designated this unique $A_{O'}B_O$ pair of $eA_3B_3$ as 'bindable' form.

The reason that the empty form cannot bind AMP-PNP:Mg whereas the bindable form can is discussed here. The binding sites of empty and bindable forms are very similar except for the topologies of the Arg-fingers (Arg 350): the Arg-finger of closed Eh-B ($B_C$) in the empty conformation was closer to Arg 262 than that of open Eh-B ($B_O$) in the bindable conformation (Fig. 1i, j, red and blue boxes), which may prevent AMP-PNP:Mg binding. The conformation of Eh-B may regulate ATP-binding affinity by the Arg-finger (Arg 350) at the binding sites. Thus, these asymmetric structures suggest that the formation of the $A_3B_3$ hexamer ring imposes a restriction (stress) on the Eh-AB pair to induce conformational changes (strains) that cooperatively generate one empty (ATP-unbound form), one bindable (ATP-accessible form) and one bound (ATP-bound form) conformation, which in turn determines the order of nucleotide binding in the ring in the right-handed rotational orientation viewed from the top of the $V_1$ complex.

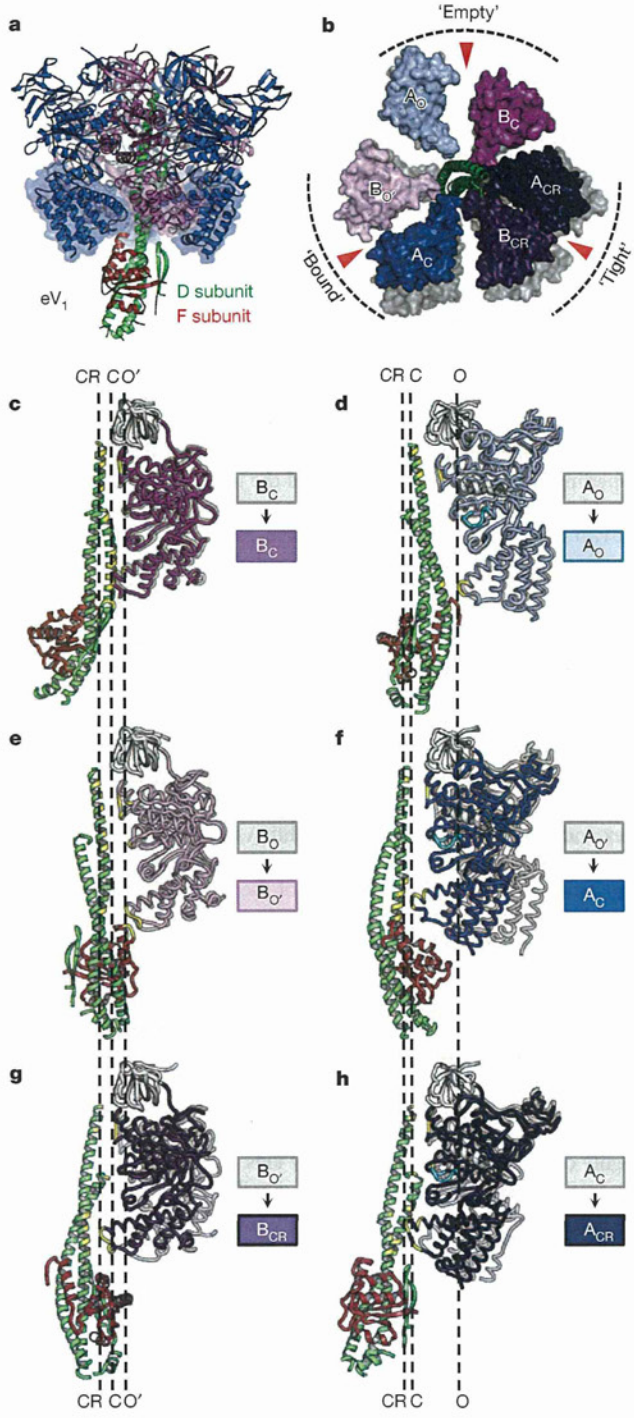


**Figure 2 | Comparison of the asymmetric structures of nucleotide-free $A_3B_3DF$ and $A_3B_3$ complexes.** **a**, Side view of the nucleotide-free $A_3B_3DF$ structure ($eV_1$). **b**, Top views of the C-terminal domain of $eV_1$ as in Fig. 1d, which is superimposed at the empty form onto that of transparent $eA_3B_3$ (grey). Open (O and O'), closed (C) and closer (CR) conformations of Eh-A and -B are shown in light, dark and darker colours, respectively. **c–h**, Protein–protein interactions between $A_3B_3$ and DF in $eV_1$. The $B_C$ (**c**), $A_O$ (**d**), $B_{O'}$ (**e**), $A_C$ (**f**), $B_{CR}$ (**g**) and $A_{CR}$ (**h**) with DF complex in $eV_1$ are shown in side-viewed ribbon representation, which are compared with corresponding subunits (grey) of $eA_3B_3$ superimposed as in **b**. The P-loop is shown in cyan. The residues with buried surface area >10 Å$^2$, as calculated by PDBePISA (http://pdbe.org/pisa/), are shown in yellow.

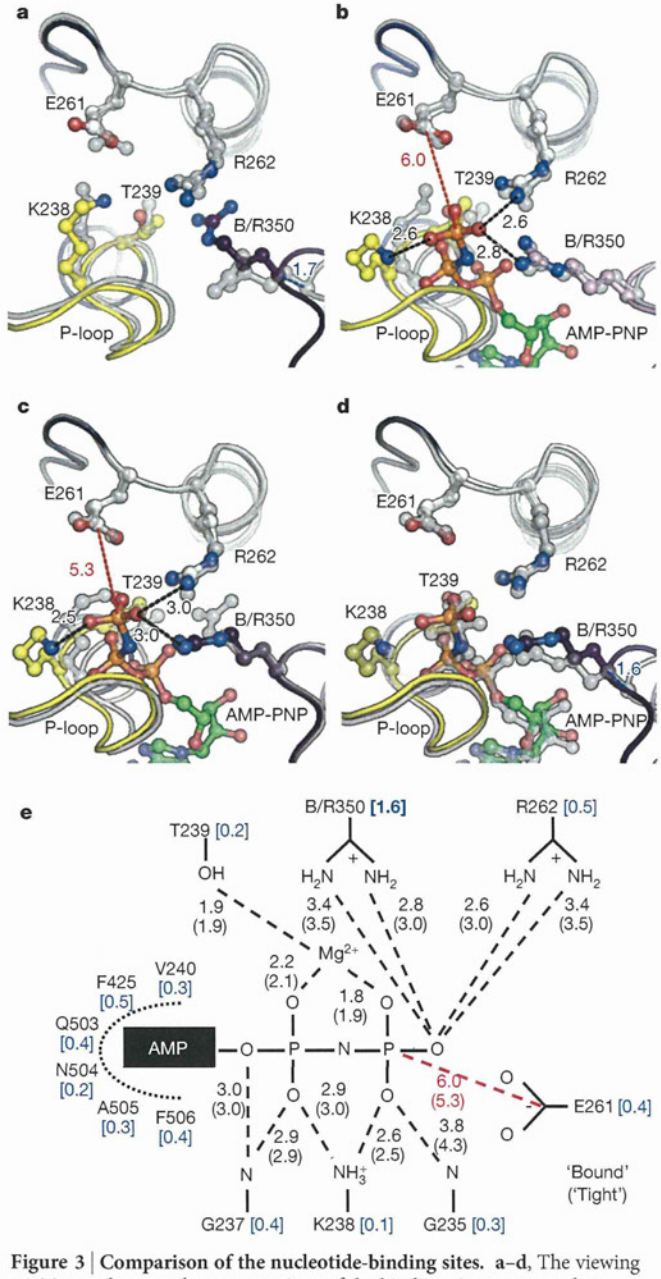


**Figure 3 | Comparison of the nucleotide-binding sites.** **a–d**, The viewing position, colours and representations of the binding site correspond to those of the right columns in Fig. 1i–l. These structures were superimposed at Eh-A (residues 67–593) of the compared AB pairs. **a**, Tight form in $eV_1$ (colour) compared with bound form in $eA_3B_3$ (grey). **b**, Bound form in $bV_1$ (colour) compared with bound form in $eV_1$ (grey). **c**, Tight form in $bV_1$ (colour) compared with tight form in $eV_1$ (grey). **d**, Tight form in $bV_1$ (colour) compared with bound form in $bV_1$ (grey). The distances (Å) between atoms are shown with dotted lines. **e**, A schematic representation of the nucleotide-binding sites of $bV_1$. The distances (Å) between atoms in the bound form or tight form (shown in parentheses) are shown with dotted lines. The distances (Å) between Cαs in the superimposed structure (**d**) are shown in blue brackets.

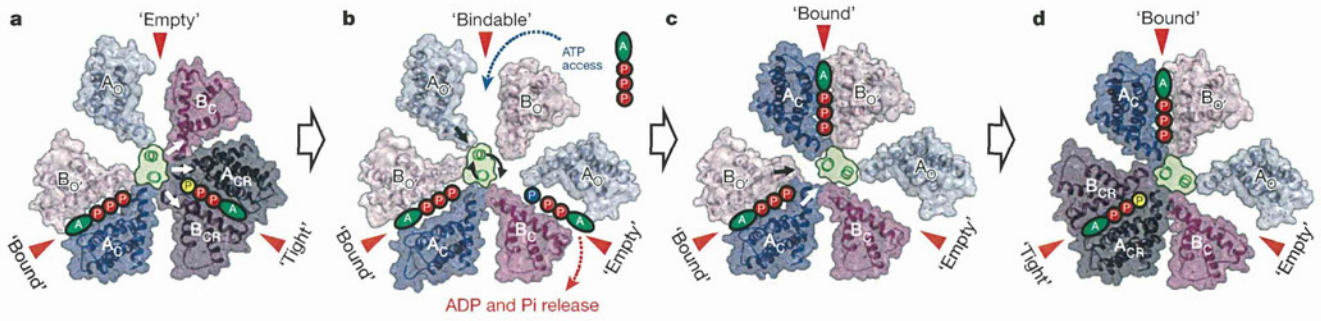


**Figure 4 | A model of the rotation mechanism of $V_1$-ATPase.** **a–d**, The structure models are on the basis of the crystal structures of $bV_1$ (**a** and **d**), $eA_3B_3$ (**b**) and $bA_3B_3$ (**c**) in this study. ATP with yellow 'P' in **a** and **d** represents an ATP molecule that is committed to hydrolysis. The blue 'P' in **b** represents a Pi molecule after hydrolysis of ATP. See text for further details.

Next, we crystallized and solved the crystal structure of the nucleotide-free $V_1$-ATPase (denoted as $eV_1$) at 2.2 Å resolution (see Supplementary Figs 9–11 and Supplementary Discussion for details). Eh-A and Eh-B assembled asymmetrically, similar to the $A_3B_3$ complex, and a central axis composed of Eh-D and Eh-F penetrated into the cavity of the $A_3B_3$ hexamer (Fig. 2a). Eh-D demonstrated a straighter conformation compared with that of the crystal structure of the DF complex[3], but other features were very similar (Supplementary Fig. 12). The coiled-coil α-helices of Eh-D interacted with several residues inside the $A_3B_3$ complex by forming 19 polar interactions and 101 non-polar (van der Waals) interactions (Fig. 2c–h and Supplementary Fig. 13).

The structural differences between $eA_3B_3$ and $eV_1$ that should have been induced by interaction with the DF complex are compared in Fig. 2. The $eV_1$ had an empty form ($A_OB_C$) (r.m.s.d = 0.544 Å) and a bound form ($A_CB_{O'}$) (r.m.s.d. = 0.699 Å), but the $eV_1$-bound form was positioned as the site of the $eA_3B_3$-bindable form when both empty forms were superimposed (Figs 1d and 2b and Supplementary Fig. 14). Therefore, the DF binding seemed to induce a change from the bindable form ($A_{O'}B_O$) of $eA_3B_3$ to the bound form ($A_CB_{O'}$), similar to the conformational changes of the $eA_3B_3$ induced by AMP-PNP binding (see Supplementary Videos 1 and 2). The remaining AB pair of $eV_1$ represented a more tightly packed conformation composed of closer Eh-A and -B conformations approaching the centre of the $A_3B_3$ ring, and this was not observed in the structure of the $A_3B_3$ complex (Fig. 2g, h). We designated these new conformations of closer Eh-A and -B subunits and the tightly packed Eh-AB pair as the $A_{CR}$ and $B_{CR}$ subunits and 'tight' form, respectively. Therefore, DF complex binding seemed to change the bound form ($A_CB_{O'}$) of $eA_3B_3$ to the tight form ($A_{CR}B_{CR}$) by interacting with several Eh-A and -B residues (Fig. 2g, h and Supplementary Video 2).

These observations raise an intriguing question about the nature of the tight form, which occurs from the bound form by interaction with the DF complex. Figure 3a shows the nucleotide-binding site of the tight form ($A_{CR}B_{CR}$) of $eV_1$, which was compared with that of the bound form ($A_CB_{O'}$) of $eA_3B_3$. In particular, the Arg-finger (Arg 350) of $B_{CR}$ approached 1.7 Å closer to Arg 262 relative to that of $B_{O'}$ (Fig. 3a, blue dotted line). Thus, obtaining the structure of the nucleotide-bound $V_1$-ATPase is essential to understanding the effect of Arg-finger movement to the nucleotide. Crystals of $eV_1$ were soaked in crystallization buffer with 200 μM AMP-PNP:Mg (a concentration sufficient to inhibit activity), and the crystal structure of the nucleotide-bound $V_1$-ATPase (denoted as $bV_1$) was solved to a resolution of 2.7 Å (Supplementary Table 2). The overall structure was very similar to that of $eV_1$ (r.m.s.d. = 0.913 Å). A strong electron density peak for AMP-PNP:Mg was observed in the binding site of the bound and tight forms, but not in the empty form (Supplementary Fig. 15), indicating that the empty form has a low affinity for AMP-PNP:Mg, consistent with the observation of the empty form in $bA_3B_3$.

The γ-phosphate of AMP-PNP and $Mg^{2+}$ were fixed by the Eh-A side chains of Lys 238, Thr 239 and Arg 262 and the Arg-finger (Arg 350) of Eh-B, similar to those of $bA_3B_3$ (Fig. 3 and Supplementary Video 3). Superimposition of the binding site of the tight form onto that of the bound form in $bV_1$ revealed small but significant differences between the two sites (Fig. 3b–e). In the tight form, movement of the Arg-finger (Arg 350) 1.6 Å closer to the γ-phosphate relative to the bound form (Fig. 3d, blue dotted line) caused the rotation of the AMP-PNP γ-phosphate. Subsequently, the γ-phosphate moved 0.7 Å closer to the conserved Glu 261 (see Supplementary Video 4), which is a crucial residue for hydrolysis of yeast $V_1$-ATPase[29]; the corresponding residue of $F_1$-ATPase interacts with the γ-phosphate oxygen of ATP via a water molecule and is assumed to cleave the β-γ bond of ATP directly[6,9,10,30]. These findings suggest that hydrolysis of ATP is stimulated by this approach triggered by movement of the Arg-finger, which is induced by extensive protein–protein interactions between the DF complex and the C-terminal domains of Eh-A and Eh-B. To confirm the importance of the Arg-finger of Eh-B in ATP hydrolysis, we constructed three site-directed mutants of the Arg-finger and examined their biochemical properties (see Supplementary Table 3). The biochemical findings are consistent with the structural findings, in which hydrolysis of ATP is predicted to occur in the tight form induced by the Arg-finger approaching towards ATP. Therefore, we concluded that the obtained structure of $bV_1$ represents an intermediate state of waiting for ATP hydrolysis in the catalytic cycle of $V_1$-ATPase.

The structures and conformational differences of the three Eh-A or B subunits are apparently different from those of the $F_1$-ATPases, although the nucleotide-binding-site structures of these ATPases are highly conserved (see Supplementary Figs 16, 17 and Supplementary Discussion). Here we summarize a possible model of the rotation mechanism of $V_1$-ATPase based on the asymmetric crystal structures in this study. Figure 4a shows the structure of the C-terminal domain surface of $bV_1$ viewed from the top, in which two ATP:Mg molecules are bound in the bound and tight forms. Bound ATP in the tight form is awaiting ATP hydrolysis as described above. Hydrolysis of ATP seems to initiate the reaction as a trigger. New ATP molecules are unable to bind to the empty form because of its low affinity for ATP. Therefore, to continue the reaction, certain structural changes in the tight form should be induced by the conversion to ADP and Pi. If the effects of DF binding are ignored, the conformation of $A_3B_3$ in $V_1$-ATPase may change (return) to $eA_3B_3$ (ground structure of $A_3B_3$ complex) in a cooperative manner, as shown in Fig. 4b: the bound form remains stabilized by the bound ATP:Mg, the empty and tight forms in $V_1$ may change to the bindable form able to bind ATP and the empty form with low affinity for ATP, respectively. However, the extensive protein–protein interactions between the DF and $A_{CR}B_{CR}$ pair (tight form) may prevent this conformational change within the $A_3B_3$, indicating that an intermediate state should exist in place of the state of Fig. 4b. In the next step, the rotation of the DF complex seems

to be induced by ATP binding to the bindable form, or to the corresponding conformation in the intermediate state in which Eh-B, with its Arg-finger, seems to adopt an open conformation similar to $B_O$ to enable ATP binding. Subsequently, the conformation changes to $bA_3B_3$, which binds ATP:Mg molecules in two bound forms, and the DF complex rotates (Fig. 4c). Finally, the older bound form changes to the tight form, induced by DF binding (Fig. 4d and Supplementary Video 3). Simultaneously, hydrolysis of ATP is again enhanced by the approach of the Arg-finger caused by the conformational change, and the enzyme reverts to its initial state, as in Fig. 4a. To understand the rotational mechanism of $V_1$-ATPase more precisely, further investigations should be undertaken, such as additional structural studies, molecular simulations and single-molecule observation of the rotation.

## METHODS SUMMARY

**Sample preparation.** The $A_3B_3$ and DF complexes of *E. hirae* were expressed using an *Escherichia coli* cell-free protein expression system and purified as previously described[2,3]. Eh-$V_1$ ($A_3B_3$DF) was purified by gel filtration after incubation of Eh-$A_3B_3$ with an excess concentration (fivefold) of Eh-DF.

**Crystallization, data collection and structure determination.** Crystals of nucleotide-free $A_3B_3$ ($eA_3B_3$), nucleotide-bound $A_3B_3$ ($bA_3B_3$), nucleotide-free $V_1$ ($eV_1$) and nucleotide-bound $V_1$ ($bV_1$) were grown by sitting drop vapour diffusion method under the conditions described in the Methods. Diffraction data were collected from a single cryo-cooled crystal on BL41XU at SPring-8 (Harima, Japan) and NW12A, NE3A and BL1A at Photon Factory (Tsukuba, Japan). The structures of $eA_3B_3$, $bA_3B_3$ and $bV_1$ were solved by molecular replacement using the crystal structures of *T. thermophilus* $A_3B_3$ complex (PDB accession 3GQB)[19], $A_3B_3$ part in $eV_1$, and whole $eV_1$ as search models. The structure of $eV_1$ was solved by molecular replacement with single-wavelength anomalous diffraction using the structures of $eA_3B_3$ and Eh-DF (PDB accession 3AON), which were superimposed onto *T. thermophilus* $V_1$-ATPase (PDB accession 3A5C)[20]. Data collection and refinement statistics are summarized in Supplementary Tables 1 and 2.

**Full Methods** and any associated references are available in the online version of the paper.

**Received 1 May; accepted 8 November 2012.**

**Published online 13 January 2013; corrected online 30 January 2013 (see full-text HTML version for details).**

1. Forgac, M. Vacuolar ATPases: rotary proton pumps in physiology and pathophysiology. *Nature Rev. Mol. Cell Biol.* **8,** 917–929 (2007).
2. Arai, S. *et al.* Reconstitution *in vitro* of the catalytic portion (NtpA$_3$-B$_3$-D-G complex) of *Enterococcus hirae* V-type $Na^+$-ATPase. *Biochem. Biophys. Res. Commun.* **390,** 698–702 (2009).
3. Saijo, S. *et al.* Crystal structure of the central axis DF complex of the prokaryotic V-ATPase. *Proc. Natl Acad. Sci. USA* **108,** 19955–19960 (2011).
4. Walker, J. E. ATP synthesis by rotary catalysis (Nobel Lecture). *Angew. Chem. Int. Edn Engl.* **37,** 2308–2319 (1998).
5. Mulkidjanian, A. Y., Makarova, K. S., Galperin, M. Y. & Koonin, E. V. Inventing the dynamo machine: the evolution of the F-type and V-type ATPases. *Nature Rev. Microbiol.* **5,** 892–899 (2007).
6. Abrahams, J. P., Leslie, A. G., Lutter, R. & Walker, J. E. Structure at 2.8 Å resolution of F1-ATPase from bovine heart mitochondria. *Nature* **370,** 621–628 (1994).
7. Menz, R. I., Walker, J. E. & Leslie, A. G. Structure of bovine mitochondrial $F_1$-ATPase with nucleotide bound to all three catalytic sites: implications for the mechanism of rotary catalysis. *Cell* **106,** 331–341 (2001).
8. Kagawa, R., Montgomery, M. G., Braig, K., Leslie, A. G. W. & Walker, J. E. The structure of bovine $F_1$-ATPase inhibited by ADP and beryllium fluoride. *EMBO J.* **23,** 2734–2744 (2004).
9. Bowler, M. W., Montgomery, M. G., Leslie, A. G. W. & Walker, J. E. Ground state structure of $F_1$-ATPase from bovine heart mitochondria at 1.9 Å resolution. *J. Biol. Chem.* **282,** 14238–14242 (2007).
10. Kabaleeswaran, V., Puri, N., Walker, J. E., Leslie, A. G. W. & Mueller, D. M. Novel features of the rotary catalytic mechanism revealed in the structure of yeast $F_1$ ATPase. *EMBO J.* **25,** 5433–5442 (2006).
11. Kabaleeswaran, V. *et al.* Asymmetric structure of the yeast $F_1$ ATPase in the absence of bound nucleotides. *J. Biol. Chem.* **284,** 10546–10551 (2009).
12. Stock, D., Leslie, A. G. & Walker, J. E. Molecular architecture of the rotary motor in ATP synthase. *Science* **286,** 1700–1705 (1999).
13. Shirakihara, Y. *et al.* The crystal structure of the nucleotide-free $\alpha 3\beta 3$ subcomplex of $F_1$-ATPase from the thermophilic *Bacillus* PS3 is a symmetric trimer. *Structure* **5,** 825–836 (1997).
14. Cingolani, G. & Duncan, T. M. Structure of the ATP synthase catalytic complex ($F_1$) from *Escherichia coli* in an autoinhibited conformation. *Nature Struct. Mol. Biol.* **18,** 701–707 (2011).
15. Noji, H., Yasuda, R., Yoshida, M. & Kinosita, K. Direct observation of the rotation of $F_1$-ATPase. *Nature* **386,** 299–302 (1997).
16. Yasuda, R., Noji, H., Yoshida, M., Kinosita, K. & Itoh, H. Resolution of distinct rotational substeps by submillisecond kinetic analysis of $F_1$-ATPase. *Nature* **410,** 898–904 (2001).
17. Adachi, K. *et al.* Coupling of rotation and catalysis in $F_1$-ATPase revealed by single-molecule imaging and manipulation. *Cell* **130,** 309–321 (2007).
18. Toei, M. *et al.* Dodecamer rotor ring defines $H^+$/ATP ratio for ATP synthesis of prokaryotic V-ATPase from *Thermus thermophilus*. *Proc. Natl Acad. Sci. USA* **104,** 20256–20261 (2007).
19. Maher, M. J. *et al.* Crystal structure of $A_3B_3$ complex of V-ATPase from *Thermus thermophilus*. *EMBO J.* **28,** 3771–3779 (2009).
20. Numoto, N., Hasegawa, Y., Takeda, K. & Miki, K. Inter-subunit interaction and quaternary rearrangement defined by the central stalk of prokaryotic $V_1$-ATPase. *EMBO Rep.* **10,** 1228–1234 (2009).
21. Imamura, H. *et al.* Rotation scheme of $V_1$-motor is different from that of $F_1$-motor. *Proc. Natl Acad. Sci. USA* **102,** 17929–17933 (2005).
22. Murata, T., Igarashi, K., Kakinuma, Y. & Yamato, I. $Na^+$ binding of V-type $Na^+$-ATPase in *Enterococcus hirae*. *J. Biol. Chem.* **275,** 13415–13419 (2000).
23. Murata, T., Yamato, I., Kakinuma, Y., Leslie, A. G. W. & Walker, J. E. Structure of the rotor of the V-Type $Na^+$-ATPase from *Enterococcus hirae*. *Science* **308,** 654–659 (2005).
24. Murata, T. *et al.* Ion binding and selectivity of the rotor ring of the $Na^+$-transporting V-ATPase. *Proc. Natl Acad. Sci. USA* **105,** 8607–8612 (2008).
25. Mizutani, K. *et al.* Structure of the rotor ring modified with N,N-dicyclohexylcarbodiimide of the $Na^+$-transporting vacuolar ATPase. *Proc. Natl Acad. Sci. USA* **108,** 13474–13479 (2011).
26. Murata, T., Yamato, I. & Kakinuma, Y. Structure and mechanism of vacuolar $Na^+$-translocating ATPase from *Enterococcus hirae*. *J. Bioenerg. Biomembr.* **37,** 411–413 (2005).
27. Yamamoto, M. *et al.* Interaction and stoichiometry of the peripheral stalk subunits NtpE and NtpF and the N-terminal hydrophilic domain of NtpI of *Enterococcus hirae* V-ATPase. *J. Biol. Chem.* **283,** 19422–19431 (2008).
28. Zhou, M. *et al.* Mass spectrometry of intact V-type ATPases reveals bound lipids and the effects of nucleotide binding. *Science* **334,** 380–385 (2011).
29. Liu, Q. *et al.* Site-directed mutagenesis of the yeast V-ATPase A subunit. *J. Biol. Chem.* **272,** 11750–11756 (1997).
30. Dittrich, M., Hayashi, S. & Schulten, K. On the mechanism of ATP hydrolysis in $F_1$-ATPase. *Biophys. J.* **85,** 2253–2266 (2003).

**Supplementary Information** is available in the online version of the paper.

**Acknowledgements** We thank J. E. Walker for his suggestions, especially through the structural studies of $F_1$-ATPase. The synchrotron radiation experiments were performed at SPring-8 and Photon Factory (proposals 2008S2-001, 2011S2-005, 2009G660, 2009B1031 and 2012G132). We also thank the beamline staff at BL41XU of SPring-8 (Harima, Japan) and NE3A, NW12A and BL1A of Photon Factory (Tsukuba, Japan) for help during data collection. This work was supported by the Targeted Proteins Research Program, grants-in-aid (23370047, 23118705), Special Coordination Funds for Promoting Science and Technology from the Ministry of Education, Culture, Sports, Science and Technology of the Japanese government.

**Author Contributions** T.M. designed the study. S.A., Y.K. and N.O. constructed DNAs. Y.I.-K., T.T. and M.S. expressed and purified the proteins. K.S. and T.M. crystallized the proteins. S.A., S.S., K.S., K.M. and T.M. collected X-ray data. S.A., S.S. and K.M. processed and refined X-ray data. S.A. and K.S. performed functional analysis. S.A., S.S., I.Y. and T.M. analysed the results. S.A. and S.S. prepared figures and videos. T.M. wrote the paper. All authors discussed the results and commented on the manuscript. The study was managed by S.Y., S.I., I.Y. and T.M.

**Author Information** Atomic coordinates and structure factors for the $A_3B_3$ and $V_1$-ATPase complexes have been deposited in the Protein Data Bank under the accession codes 3VR2 (nucleotide-free $A_3B_3$ at 2.8 Å), 3VR3 (nucleotide-bound $A_3B_3$ at 3.4 Å), 3VR4 (nucleotide-free $V_1$-ATPase at 2.2 Å), 3VR5 (nucleotide-free $V_1$-ATPase at 3.9 Å) and 3VR6 (nucleotide-bound $V_1$-ATPase at 2.7 Å). Reprints and permissions information is available at www.nature.com/reprints. The authors declare no competing financial interests. Readers are welcome to comment on the online version of the paper. Correspondence and requests for materials should be addressed to T.M. (t.murata@faculty.chiba-u.jp).

## METHODS

**Protein preparation.** An *Escherichia coli* cell-free protein expression system, as described elsewhere[31], was used to synthesize the Eh-$A_3B_3$ and DF complexes using a mixture of plasmids containing the corresponding genes. The expressed complexes were purified as previously described[2,3]. Selenomethionine-labelled Eh-$A_3B_3$ and DF complexes were also prepared to facilitate X-ray structure determination. The sum of ATP and ADP contamination in 0.5 μM purified Eh-$A_3B_3$ and DF complexes (denatured with 0.6 M perchloric acid) was estimated with a luciferin–luciferase assay[32], after conversion of ADP to ATP using an ATP regeneration system[3] for 30 min at room temperature; ATP and ADP contamination was undetectable (less than 0.1 nM). The $V_1$-ATPase (Eh-$A_3B_3$DF) was reconstituted and purified as follows: purified Eh-$A_3B_3$ and Eh-DF in buffer A (20 mM Tris-HCl, pH 8.0, 150 mM NaCl and 2 mM dithiothreitol (DTT)) were mixed at a 1:5 molar ratio with the addition of MES (100 mM final concentration; pH 6.0), and were incubated with and without 0.2 mM AMP-PNP and 5 mM $MgSO_4$ for 1 h. Reconstituted $V_1$-ATPase with and without AMP-PNP:Mg was purified using a HiLoad 16/60 Superdex 200 (GE Healthcare) column equilibrated with buffer B (20 mM MES, pH 6.5, 10% glycerol, 100 mM NaCl, 5 mM $MgSO_4$ and 2 mM DTT), respectively. Purified complexes were concentrated with an Amicon Ultra 30 K unit (Merck Millipore).

**Protein crystallization.** All crystallization trials were performed using the sitting-drop vapour diffusion method at 296 K. The crystals were soaked in cryoprotectant by incrementally increasing the glycerol concentration to 20%. The crystals were then mounted on cryo-loops (Hampton Research), flash-cooled and stored in liquid nitrogen.

(1) Eh-$A_3B_3$ without nucleotide (e$A_3B_3$): Eh-$A_3B_3$ crystals were obtained by mixing 0.5 μl protein solution (12 mg ml$^{-1}$ protein in buffer A) with 0.5 μl reservoir solution (0.1 M MES-Tris, pH 8.5, 24% PEG-3350 and 0.2 M ammonium acetate).

(2) Eh-$A_3B_3$ with AMP-PNP:Mg (b$A_3B_3$): Eh-$A_3B_3$ crystals were obtained by mixing 0.5 μl protein solution (11 mg ml$^{-1}$ protein in buffer A) supplemented with 5 mM AMP-PNP and 5 mM $MgSO_4$ with 0.5 μl reservoir solution (0.1 M HEPES, pH 7.5, 26% PEG-3350, and 0.2 M sodium chloride).

(3) $V_1$-ATPase with AMP-PNP:Mg (e$V_1$): $V_1$ crystals were obtained by mixing 0.5 μl protein solution (12 mg ml$^{-1}$ protein in the presence of 0.2 mM AMP-PNP in buffer B) with 0.5 μl reservoir solution (0.1 M Bis-Tris propane, pH 6.5, 19% PEG-3350 and 0.2 M sodium fluoride).

(4) $V_1$-ATPase without nucleotide (e$V_1$(L)): $V_1$ crystals were obtained by mixing 0.5 μl protein solution (10 mg ml$^{-1}$ protein in buffer B) with 0.5 μl reservoir solution (0.1 M Bis-Tris propane, pH 6.5, 20% PEG-3350 and 0.2 M sodium fluoride).

(5) $V_1$-ATPase soaked with AMP-PNP:Mg (b$V_1$): $V_1$ crystals that were obtained in (3) were soaked for 5 h in 0.1 M Bis-Tris propane, pH 6.5, 21% PEG-3350, 0.2 mM AMP-PNP (a concentration sufficient to inhibit the activity), 3 mM $MgSO_4$, 0.2 M sodium chloride (replaced for sodium fluoride) and 20% glycerol.

**Structure determination.** All X-ray diffraction data were collected from a single crystal at a cryogenic temperature (100 K).

(1) Eh-$A_3B_3$ without nucleotide (e$A_3B_3$): X-ray diffraction data were collected on beamline BL41XU ($\lambda = 1.0000$ Å) at SPring-8 (Harima, Japan). The collected data were processed to 2.8 Å using iMosflm[33] and then scaled by Scala from the *CCP*4 program suite[34]. The structure was solved by molecular replacement with MOLREP[35] using the poly-Ser model of $A_3B_3$ complex from *T. thermophilus* (PDB accession 3GQB)[19] as a search model.

(2) Eh-$A_3B_3$ with AMP-PNP:Mg (b$A_3B_3$): X-ray diffraction data were collected on beamline BL41XU ($\lambda = 1.0000$ Å) at SPring-8. The collected data were processed to 3.4 Å using iMosflm[33] and then scaled by Scala[34]. The structure was solved by molecular replacement with MOLREP[35] using the structure of Eh-$A_3B_3$ in e$V_1$ as a search model.

(3) $V_1$-ATPase with AMP-PNP:Mg (e$V_1$): X-ray diffraction data were collected on beamline NW12A ($\lambda = 0.97919$ and 1.0000 Å) at Photon Factory (Tsukuba, Japan). The collected data were processed and scaled to 2.6 and 2.2 Å using XDS[36]. The structure was solved by MR–SAD (molecular replacement with single-wavelength anomalous diffraction) using Phaser[37]. The partially refined A and B subunits from the structure of Eh-$A_3B_3$ without nucleotide and the DF complex from *E. hirae* (PDB accession 3AON) were superimposed onto the $V_1$-ATPase from *T. thermophilus* (PDB accession 3A5C)[20]. The superimposed model was used as an initial search model. The overall figure of merit (FOM = $\Sigma P(\alpha) \exp(i\alpha)/\Sigma P(\alpha)$, in which $P(\alpha)$ is the probability distribution for the phase($\alpha$)) was 0.45 using combined phases of SAD from selenium and molecular replacement at 3.0 Å.

(4) $V_1$-ATPase without nucleotide (e$V_1$(L)): X-ray diffraction data were collected on beamline NE3A ($\lambda = 1.0000$ Å) at Photon Factory. The collected data were processed to 3.9 Å using XDS. The structure was solved by molecular replacement with Phaser using the crystal structure of e$V_1$ as a search model.

(5) $V_1$-ATPase soaked with AMP-PNP:Mg (b$V_1$): X-ray diffraction data were collected on beamline BL1A ($\lambda = 1.0000$ Å) at Photon Factory. The collected data were processed to 2.7 Å using HKL2000 software (HKL Research). The structure was solved by molecular replacement with MOLREP using the crystal structure of e$V_1$ as a search model.

The atomic models were manually built using Coot[38] and iteratively refined using REFMAC5[39] (REFMAC5 and PHENIX[40] were used for refinement of e$V_1$). The refined structures were validated with PROCHECK[41] and RAMPAGE[42]. The crystallographic and refinement statistics are summarized in Supplementary Tables 1 and 2. The r.m.s.d. values of superimpositions for each Eh-A, Eh-B or Eh-AB pair in the crystal structures of $A_3B_3$ and $V_1$-ATPase are listed in Supplementary Tables 4 and 5. Figures were prepared using PyMOL (The PyMOL Molecular Graphics System, Version 1.3, Schrodinger, LLC.)

**Characterization of the Arg-finger mutants.** Mutagenesis of the Arg-finger (Arg350Ala/Glu/Lys) of Eh-B was performed using the QuikChange site-directed mutagenesis kit (Agilent Technologies). The Arg350Ala Eh-B mutant could not be purified as a complex with Eh-A. The other mutants were purified as described above. Binding affinities between the Eh-$A_3B_3$ mutants and the DF complex were measured using the Biacore T100 system (GE Healthcare) as described previously[3]. The dissociation constant ($K_d$) was determined using BIAevaluation software (version 1.1), which uses the Langmuir isotherm model that assumes a 1:1 binding stoichiometry. ATPase activity was measured according to a previous report using the ATP-regeneration system[3].


31. Kigawa, T. *et al.* Preparation of *Escherichia coli* cell extract for highly productive cell-free protein expression. *J. Struct. Funct. Genomics* **5,** 63–68 (2004).
32. Deluca, M. & McElroy, W. D. Purification and properties of firefly luciferase. *Methods Enzymol.* **57,** 3–15 (1978).
33. Battye, T. G. G., Kontogiannis, L., Johnson, O., Powell, H. R. & Leslie, A. G. W. iMOSFLM: a new graphical interface for diffraction-image processing with MOSFLM. *Acta Crystallogr. D* **67,** 271–281 (2011).
34. Collaborative Computational Project, Number 4. The *CCP*4 suite: programs for protein crystallography. *Acta Crystallogr. D* **50,** 760–763 (1994).
35. Vagin, A. & Teplyakov, A. Molecular replacement with MOLREP. *Acta Crystallogr. D* **66,** 22–25 (2010).
36. Kabsch, W. XDS. *Acta Crystallogr. D* **66,** 125–132 (2010).
37. McCoy, A. J. *et al.* Phaser crystallographic software. *J. Appl. Crystallogr.* **40,** 658–674 (2007).
38. Emsley, P. & Cowtan, K. Coot: model-building tools for molecular graphics. *Acta Crystallogr. D* **60,** 2126–2132 (2004).
39. Murshudov, G. N., Vagin, A. A. & Dodson, E. J. Refinement of macromolecular structures by the maximum-likelihood method. *Acta Crystallogr. D* **53,** 240–255 (1997).
40. Adams, P. D. *et al.* PHENIX: a comprehensive Python-based system for macromolecular structure solution. *Acta Crystallogr. D* **66,** 213–221 (2010).
41. Laskowski, R. A., MacArthur, M. W. & Thornton, J. M. Validation of protein models derived from experiment. *Curr. Opin. Struct. Biol.* **8,** 631–639 (1998).
42. Lovell, S. C. *et al.* Structure validation by Cα geometry: ϕ, ψ and Cβ deviation. *Proteins* **50,** 437–450 (2003).